IOP Publishing Measurement Science and Technology
Meas. Sci. Technol. **31** (2020) 055301 (34pp) https://doi.org/10.1088/1361-6501/ab6c28

Error propagation from the PIV-based pressure gradient to the integrated pressure by the omnidirectional integration method

Xiaofeng Liu[1] **and Jose Roberto Moreto**[2]

[1] Department of Aerospace Engineering, San Diego State University, Associate Fellow AIAA, San Diego, CA 92182-1308, United States of America
[2] San Diego State University-University of California San Diego, Joint Doctoral Program in Aerospace Engineering, San Diego, CA 92182-1308, United States of America

E-mail: xiaofeng.liu@sdsu.edu

Received 10 June 2019, revised 12 January 2020
Accepted for publication 15 January 2020
Published 6 February 2020

Abstract

This paper reports a theoretical analysis and the corresponding numerical and experimental validation results of the error propagation characteristics of the omnidirectional integration method used for pressure reconstruction from the PIV measured pressure gradient. The analysis shows that the omnidirectional integration provides an effective mechanism in reducing the sensitivity of the reconstructed pressure to the random noise embedded in the measured pressure gradient. Accurate determination of the boundary pressure values is the first step in ensuring the accuracy of the reconstructed pressure. The boundary pressure error consists of two parts, with one part decreasing exponentially in magnitude and eventually vanishing, and the other remaining as a constant with small magnitude through iteration. These results are verified by using a direct numerical simulation database of isotropic turbulence flow superimposed with noise at various noise levels and spatial distribution schemes to simulate noise embedded data. The nondimensionalized average error of the reconstructed pressure based on 1000 statistically independent pressure gradient field realizations with a 40% added noise level is 0.854 ± 0.406 for the pressure Poisson equation with Neumann boundary condition, 0.154 ± 0.015 for the circular virtual boundary omnidirectional integration and 0.149 ± 0.015 for the rotating parallel ray omnidirectional integration. If the converged boundary pressure values obtained by the rotating parallel ray are used as Dirichlet boundary conditions, the average pressure error by Poisson is reduced to 0.151 ± 0.015. Of the different variations of the omnidirectional methods, the parallel ray method shows the best performance and therefore is the method of choice. Comparisons of the performance of these pressure reconstruction methods using an experimentally obtained turbulent shear layer flow over an open cavity are in agreement with the conclusions obtained with the DNS simulation data. With the noise added DNS data, limitations regarding the pressure reconstruction methods in determining pressure fluctuation statistics are also identified and quantified.

Keywords: pressure, pressure reconstruction, pressure gradient, boundary condition, error-embedded data, Poisson equation.

(Some figures may appear in colour only in the online journal)

 © 2020 IOP Publishing Ltd Printed in the UK

1. Introduction

Pressure, defined as the normal force per unit area acting on an arbitrarily oriented surface (either virtual or real) within the fluid flow field, is an important fluid flow property that plays a crucial role in the description and modelling of a variety of flow phenomena. For example, in unsteady and turbulent flows, pressure fluctuations on solid walls often result in flow-induced vibrations and acoustic noise [1]. In turbulence research, the pressure diffusion and the pressure-strain tensors are key unresolved parameters in modelling of turbulence [2–4]. In hydrodynamics research, pressure is essential for understanding and modelling cavitation [5, 6]. Pressure is also of paramount importance in characterizing the performance of engineering systems operating in fluids. For example, the lift and the form drag acting on a moving body in fluid depends on the pressure distribution around it due to relative flow motion.

Because of the importance of the pressure information in flow field, efforts in developing non-intrusive pressure measurement techniques have been carried out in the past decade in the fluids community. Motivated by the lack of appropriate means for instantaneous spatial pressure distribution measurements, Liu and Katz [7, 8] introduced a non-intrusive technique capable of measuring the instantaneous velocity, material acceleration and spatial pressure distributions simultaneously over a sample area in a turbulent flow field. With the viscous term being negligible for high Reynolds number flow in regions away from the wall, the material acceleration is the dominant term that balances the pressure gradient. Once the material acceleration is obtained experimentally, the pressure gradient is known. Further integrating it will obtain the pressure. The material acceleration can be measured non-intrusively using particle image velocimetry (PIV), either discretely [7–10] or continuously [11–14] time-resolved.

For pressure reconstruction from the measured pressure gradient (dominated by the material acceleration), at present there are three major types of integration methods, i.e. direct line integration, Poisson equation and least-square reconstruction. For direct line integration, representative method is the so-called circular virtual boundary, omnidirectional integration [7–10, 12] over the entire measurement domain, which has evolved recently to a new algorithm featuring rotating parallel ray [15] as integration path guidance. This new 'rotating parallel ray' omnidirectional integration algorithm was recently successfully applied to 3D pressure reconstruction based on time-resolved tomographic PIV measurement of a turbulent channel flow over compliant wall [16]. A simplified multiple-line integration approach was proposed by Dabiri *et al* [17], in which the pressure was reconstructed using median polling of the integration results along several integration paths originated from typically eight surrounding directions. However, as demonstrated by Wang *et al* [18], the eight-path integration of Dabiri *et al* [17], suffers from a considerable compromise in pressure reconstruction accuracy in comparison with Liu and Katz's omnidirectional approach, although the amount of computation of the former is significantly reduced when compared with the latter.

Representative Poisson equation approach can be found in de Kat and Van Oudheusden [19, 20] and Violato *et al* [21], which use a Poisson equation solver to calculate the pressure from time resolved PIV measurements (see also [22]). More recently, an improved Poisson equation approach is proposed by Auteri *et al* [23]. Following the advent of time-resolved PIV, the pressure reconstruction has also been adapted for measuring the temporal derivatives of surface pressure distribution, which is further used for estimating the acoustic pressure radiated from a surface [24–27].

In addition to the omnidirectional integration and the Poisson equation approaches, recently a so-called least-square reconstruction approach [28] was used for experimentally obtaining instantaneous pressure field in a wake of a separated flow over an airfoil. This approach was also referred to as direct matrix inversion by Liu and Katz [7]. Actually, as demonstrated by Wang *et al* [29], the least-square approach is mathematically equivalent to the Poisson equation approach with Neumann boundary conditions.

In addition to the above integration approaches, recently several new methods were also introduced for pressure reconstruction. For example, with time-resolved 3D3C velocity field data available, Tronchin *et al* [30], demonstrated the feasibility of using a conventional CFD pressure reconstruction approach to iteratively solve the discretized Eulerian-based Navier–Stokes equation over a 'chimera mesh,' treating the pressure as an unknown quantity and the measured velocity components as the known ones. Using a Poisson solver, Neeteson and Rival [31], proposed a Lagrangian finite-volume method to obtain pressure values at particle positions determined by the Shake The Box (STB) algorithm [32]. In contrast to the conventional Poisson approach, Huhn *et al* [33], introduced a method of 3D pressure field reconstruction in the Fourier space using a fast Fourier transform (FFT) method. Exploiting the curl-free property of the pressure gradient as a constraint, Wang *et al* [18], developed a proper orthogonal decomposition (POD)–based pressure reconstruction approach, with the curl-free constrained POD as an error reduction treatment and the simple cross-line integration as the final step for obtaining the pressure.

Obviously, characterization of the accuracy of the pressure reconstruction methods is of critical importance in understanding the capabilities and limitations of these methods. There are a few studies dedicated to the evaluation of the accuracy of the pressure reconstruction methods as well as the characterization of the error propagation properties from the velocity field or acceleration field to the reconstructed pressure field. One of the first such studies was performed by Charonko *et al* [34], in which the accuracies of several methods including the Poisson equation approach, line integration, the omnidirectional integration and three smoothing methods were compared using a decaying Taylor vortex flow and two simulated pulsatile flow fields. By considering the effects of grid resolution, sampling rate, out of plane velocities and noise embedded in the velocity field, Charonko *et al* [34], found that the omnidirectional method exhibits robust performance over a wide range of resolutions, flow conditions and noise levels.

Most recently, van Gent *et al* [35], using a simulated experiment from a zonal detached eddy simulation of an axisymmetric base flow at Mach 0.7, conducted a massive comparison study for pressure reconstruction methods including the Poisson solver [19], least-square [28], FFT [33], Taylor's hypothesis and Poisson solver [36], Voronoi-Lagrangian finite-volume based Poisson solver [31]. They concluded that, although with different degrees of accuracy in reconstructed pressure distributions, all methods were able to capture the main features of the instantaneous pressure fields, including the method of de Kat and Ganapathisubramani [36], which reconstructs the pressure from a single PIV velocity snapshot based on Taylor's hypothesis for acceleration estimate.

McClure and Yarusevych [37], investigated the performance of the four pressure measurement techniques including omnidirectional [7], eight-path [17], Poisson equation, and Local least squares using direct numerical simulation data for a bluff body wake flow. The acceleration measurement approach is based on the Eulerian approach, not Lagrangian. Unfortunately, they only used five iterations for the omnidirectional pressure calculation. In comparison, the omnidirectional pressure reconstruction calculation in Liu and Katz [7, 10, 12] typically involves 60–70 times of iteration. The number of iterations makes huge difference in the accuracy of the reconstructed pressure result if the omnidirectional method is used, for reasons which will be explained in detail through an analytical analysis in this paper.

In addition to the aforementioned studies, Lynch and Scarano [38], Wieneke [39], Sciacchitano and Wieneke [40], Wang *et al* [41], Gomit *et al* [42], van Gent *et al* [43, 44] investigated influence factors such as the PIV measurement parameters and the velocity and the acceleration evaluation methods on the accuracy of the material acceleration measurement. Wang *et al* [41], evaluated analytically the uncertainty propagation from the velocity field to the material acceleration and then from the material acceleration to the pressure field. Using a probability density function to model the uncertainty in velocity and evaluate its propagation to the material acceleration for the Eulerian and Lagrangian approaches, they concluded that the error associated with Lagrangian approach is smaller than the Eulerian approach. Pan *et al* [45], performed an analytical analysis of the error propagation from the pressure gradient to the reconstructed pressure based on the Poisson equation approach. Error bounds for the error propagation indicates that the propagated error level depends on the boundary conditions, the domain shape and the error level on the pressure gradient field and boundaries. Also, the domain with pure Neumann boundary conditions needs to satisfy the compatibility condition which can be difficult for PIV. This work also lays out some guidelines for designing PIV experiments aiming to reduce error propagation to pressure measurement.

In this paper, we introduce a theoretical analysis of the error propagation from the pressure gradient to the reconstructed pressure field based on the omnidirectional integration method. To our knowledge, this is the first time that the error propagation property of the omnidirectional pressure reconstruction methods is investigated analytically. In particular, in section 2 we describe the principle of the omnidirectional integration methods and explain how they are implemented. In section 3 we derive the analytical expression for the error propagation from the pressure gradient to the reconstructed pressure for the 3D omnidirectional methods, which is valid also for the 2D omnidirectional implementation. In section 4 we evaluate and compare the error propagation and the pressure reconstruction accuracy for three approaches including the circular virtual boundary omnidirectional integration method, the parallel ray omnidirectional integration method and the conventional Poisson equation method. Please note a simplified version (Liu and Moreto [46]) of this paper was presented at ISPIV 2019 in Munich, Germany.

2. Methods

2.1. Overview

Pressure can be obtained from PIV experiments in a two-step process: first the pressure gradient is computed from the velocity fields, then the second step is the integration of the pressure gradient to obtain the pressure field. The pressure gradient can be obtained using either the Eulerian approach [19, 21, 47], where the unsteady and convection terms of the Eulerian expansion of the material acceleration are calculated directly as shown in equation (1), or the Lagrangian approach, where the material acceleration is calculated directly by tracing imaginary fluid particles along their trajectories based on the so-called pseudo tracking method [7, 19, 21, 48] as shown in equation (2):

$$\nabla p = -\rho\left[\frac{\partial \boldsymbol{u}}{\partial t} + (\boldsymbol{u}\cdot\nabla)\boldsymbol{u} - \nu\nabla^2\boldsymbol{u}\right] \tag{1}$$

$$\nabla p = -\rho\left[\frac{D\boldsymbol{u}}{Dt} - \nu\nabla^2\boldsymbol{u}\right] \tag{2}$$

For high Reynolds number flow in regions away from the wall, the viscous term is usually 3–4 orders of magnitude smaller than the pressure gradient term and therefore is negligible [7]. In this case, the pressure gradient can be determined from the measured material acceleration. The error propagation from velocity to acceleration was investigated by Jensen and Pedersen [49], Violato *et al* [21], de Kat and van Oudheusden [19], van Oudheusden [22], Wang *et al* [18], and van Gent *et al* [35]. Those investigations demonstrate that for advection dominated flows, the Lagrangian approach shows consistently less sensitivity to noise. Recently, van Gent *et al* [43, 44], by investigating the error propagation from velocity to material acceleration for the pseudo-tracking method, found that the Courant–Friedrichs–Lewy (CFL) condition that regulates the integration time step for material acceleration calculation is automatically satisfied when the PIV experiment is designed such that the particle displacement is smaller than a quarter of the interrogation window size and the interrogation window overlap is 75%. They also clarified the guiding criterion for a meaningful spectral representation of the material acceleration data in terms of the PIV window size and the pseudo-track time interval in comparison with the flow characteristic length and time scales.

To reconstruct the pressure from the pressure gradient, one can use the Poisson equation as shown in equation (3) or (4), which are obtained by taking divergence of either equation (1) or (2), respectively:

$$\nabla^2 p = -\rho\nabla\cdot\left[\frac{\partial \boldsymbol{u}}{\partial t} + (\boldsymbol{u}\cdot\nabla)\boldsymbol{u} - \nu\nabla^2\boldsymbol{u}\right] \tag{3}$$

$$\nabla^2 p = -\rho\nabla\cdot\left[\frac{D\boldsymbol{u}}{Dt} - \nu\nabla^2\boldsymbol{u}\right]. \tag{4}$$

An example of using the Poisson equation for pressure reconstruction can be found in de Kat and van Oudheusden [19], and the error bounds for the Poisson solution can be found in Pan *et al* [45]. Equations (1) and (2) can be integrated directly by means of line integrals. While several approaches were proposed to perform the line integration [7, 17, 50], the omnidirectional integration proposed by Liu and Katz [7], shows the most robust results in the assessments of Charonko *et al* [34], and Wang *et al* [18]. Moreover, a recent study by Wang *et al* [51], also demonstrated using DNS isotropic turbulence and turbulent channel flows that the new rotating parallel ray omnidirectional method [15] has better performance than the conventional Poisson equation approach.

2.2. Scope of work

How to minimize the errors embedded in the velocity measurement result and the error propagation in derived quantities based on velocity measurement is always a central theme for PIV's technological advancement. As for factors affecting the accuracy of the reconstructed pressure, besides the influences of the pressure reconstruction scheme and the pressure gradient (or acceleration) measurement scheme, errors due to velocity can always be traced back to those factors affecting the velocity measurement accuracy. For a systematic analysis of the error propagation behavior, we can divide the error propagation from velocity to reconstructed pressure into different stages, including the error generation stage in the velocity measurement, the error propagation stage from velocity to pressure gradient (acceleration) measurement, and the error propagation stage from the measured pressure gradient to the reconstructed pressure. Fortunately, error propagation within these distinguished stages are not coupled, thus allowing us to investigate the error propagation problem at different stages separately. For the error generation stage in the velocity measurement, there are numerous papers [52, 53] available in literature discussing how to minimize the influence of factors such as seeding density, correlation peak-finding scheme for achieving sub-pixel accuracy, out-of-plane motion, high velocity gradient, etc on the accuracy of the velocity measurement. For the error propagation stage from velocity to pressure gradient (acceleration) measurement, there are also abundant research efforts as mentioned before [18, 19, 21, 22, 35, 42, 43, 49] in characterizing the error propagation from PIV measured velocity to acceleration. As for the error propagation stage from the measured pressure gradient (with the measured acceleration as the dominant contributor) to the reconstructed pressure field, although previous researchers such as Pan *et al* [45], investigated the problem in the context of Poisson equation reconstructions, there is no literature available discussing about how the error is propagated from the measured pressure gradient to the reconstructed pressure using the omnidirectional methods. This paper aims to fill this gap for the first time by investigating the characteristics associated with the error propagation from the measured pressure gradient to the reconstructed pressure based on the omnidirectional integration methods introduced in Liu and Katz [7, 8, 10] and Liu *et al* [15]. Through this work, we anticipate to elucidate the mechanisms for random noise reduction that grants the robustness of the omnidirectional integration methods. To facilitate the analysis, details about the history and principle of the omnidirectional integration methods are described below.

2.3. The omnidirectional integration

The omnidirectional integration of the pressure gradient for obtaining pressure distribution from PIV experiments was proposed by Liu and Katz [8]. The integration of the measured pressure gradient is carried out by following the shortest integration paths that connect the domain boundary points across the integration domain. To determine the pressure at an internal nodal point in the field of view, the local pressure values obtained from the integration paths passing by the internal nodal point are averaged so as to minimize the influence of the error embedded in the measured pressure gradient. This method was later improved by placing a virtual boundary outside the real flow field domain and allowing the integration paths originate from and end at the virtual boundary [7] so as to reduce the path clustering close to the real boundaries. A further development was introduced by Liu and Katz [10, 12] by using a circular virtual boundary. The most recent improvement in the omnidirectional integration methods was introduced by Liu *et al* [15], using rotating parallel rays as integration guide lines.

The essence of the omnidirectional integration is to minimize the influence of the errors embedded in the measured acceleration data on the final pressure result, so as to achieve a reliable and accurate pressure measurement. The pressure integration arrangement is based on the fact that the pressure is a scalar potential, therefore the spatial integration of the pressure gradient must be independent of the integration path. As shown in figure 1(a), the discrete points distributed uniformly along the circular virtual boundary serve as guiding points to define the orientation and position of the integration paths. A group of 'virtual' integration paths start from one point and end at other points on the virtual boundary, creating a ray pattern of integration paths that cover the real field of view. The actual integration starts from and stops at the real boundaries, in a 'zig-zag' fashion, along real nodal points that have the shortest distance to the integration paths. Each time the integration path crosses a certain internal node, the result of integration is stored in a data bin associated with that internal node. This procedure is repeated for all the virtual boundary nodes. Averaging all the values stored in data bins provides the result of the omnidirectional integration.

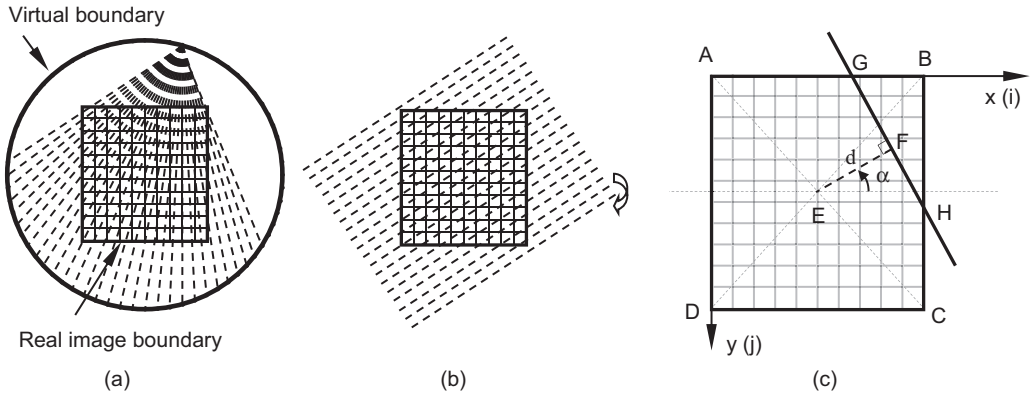

Figure 1. The omnidirectional algorithms. (a) The circular virtual boundary omnidirectional integration algorithm. (b) The rotating parallel ray omnidirectional integration algorithm. (c) Ray orientation with respect to the pressure calculation domain as a function of d (distance from the domain center) and α (ray rotation angle).

One shortcoming of the circular virtual boundary omnidirectional integration method is that except the points near the geometric center of the real integration domain, points at other places do not see an axisymmetric distribution of the virtual integration paths, which results in a non-uniform weight of contribution to the final integration result. To overcome this inherent defect, Liu *et al* [15], introduces a new algorithm featuring rotating parallel ray (figure 1(b)) as integration path guidance. Unlike the virtual boundary omnidirectional method, the new rotating parallel ray omni directional integration method utilizes parallel rays as guidance for integration paths. The parallel rays can be viewed as being originated from a virtual boundary at an infinite distance from the real boundary. Effectively, by rotating the parallel rays, omnidirectional paths with equal weights coming from all directions toward the point of interest at any location within the computation domain will be generated. In this way, the location dependence of the integration weight due to an inherent defect (though not significant) in virtual path arrangement in the old algorithm will be eliminated. As shown in figure 1(c), the orientation of the parallel rays is characterized by the angle α with respect to the horizontal direction of the pressure calculation domain. The distance between adjacent parallel rays is denoted as Δd, where d is the distance from the domain center to the ray, i.e. the guideline for the pressure reconstruction path.

For all the omnidirectional integration methods, the following procedures must be applied adequately to reduce error propagation from the boundaries.

(a) Boundary pressure calculation.
   1. Select a pressure reference point.
   2. Initialize pressure values on the boundary points by either simple line integration along boundaries or by setting the boundary pressure values to be zero.
   3. Integrate the pressure gradient field based on the specific method of the omnidirectional integration (e.g. the virtual boundary omnidirectional integration or the parallel ray omnidirectional integration).
   4. Update the boundary pressure values with the newly calculated data.
   5. Iterate until prescribed accuracy (usually on the order of 10^{-15} for the averaged pressure differences between iteration) is achieved.

(b) Inner domain pressure calculation.

3. Error propagation analysis

One primary concern for the pressure obtained from PIV measurements is its accuracy. As mentioned before, recently Pan *et al* [45], derived the error bounds for the pressure reconstruction from the Poisson solution. However, for the omnidirectional methods, there is still no theoretical analysis available about the error propagation from the pressure gradient to the reconstructed pressure. To fill in the gap, we now show the analysis of the error propagation from the pressure gradient to the reconstructed pressure by using the omnidirectional integration methods.

3.1. Pressure errors on boundary points

Assuming an error $\varepsilon_{\nabla p}$ that contaminates the measured pressure gradient field $\nabla\tilde{p}$ can be separated from the exact pressure gradient ∇p, we have

$$\nabla\tilde{p} = \nabla p + \varepsilon_{\nabla p}. \tag{5}$$

We apply the omnidirectional integration procedures described in section 2 to the integration of equation (5) over a 3D computational domain as shown in figure 2. Starting from an iterative process for the pressure determination at boundary points, we define a reference pressure at a fixed boundary point location s_r (figure 2(a)) as $\tilde{p}_r = \tilde{p}_{ref}$. We then initialize the boundary points, either by taking values of a simple line integration along boundary points starting from the reference point, or simply by setting all boundary points except the reference to zero. It turns out that, as demonstrated in figure 3 (using a 2D calculation as an example), there is no difference between the two boundary value initialization methods on the final pressure reconstruction results as long as sufficient number of iterations are involved in achieving the same prescribed

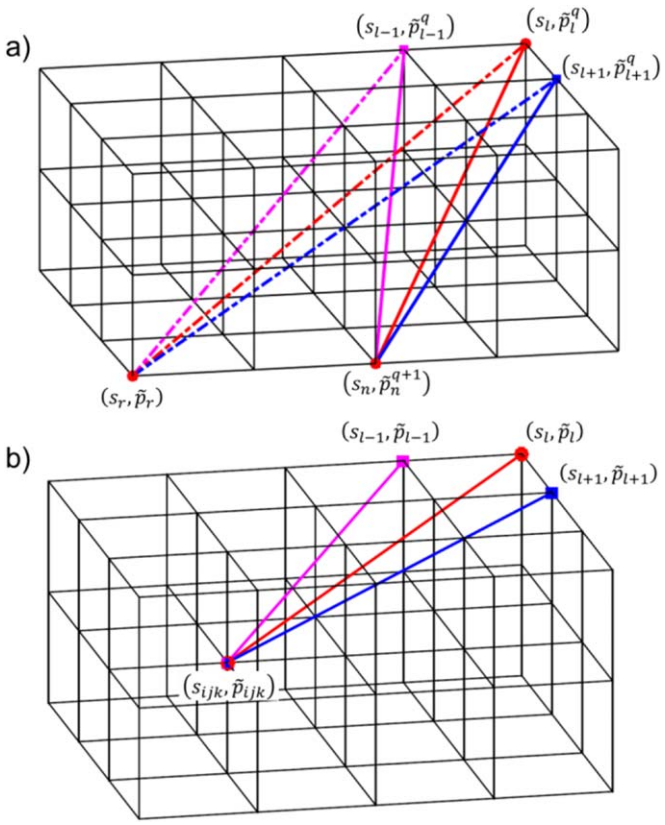

Figure 2. (a) Integration path connections among boundary points for omnidirectional integration. (b) Integration path connection between an inner nodal point and boundary points.

level of convergence for the boundary pressure value calculation. Also as shown in figure 3, even when the initial boundary pressure values are initialized with a very large number (e.g. 1.0×10^4), the final convergence can also be achieved if the number of iterations is sufficiently large enough. Please note, as shown in figure 3(a), the boundary pressure initialization method using simple line integration along boundary leads to the fastest convergence for the testing case without added noise. As a contrast, when the pressure gradient field is embedded with the 40% random noise, the approach of initialization of boundary pressure values with zeros exhibits the fastest convergence (figure 3(b)).

After initializing the boundary points, we then perform the integration to obtain converged boundary point values following the paths defined by the omnidirectional integration algorithm (e.g. the omnidirectional integration methods shown in Liu and Katz [7, 12] or Liu *et al* [15]). The pressure $\tilde{p}_n^{(q+1)}$ at an arbitrary boundary point s_n as shown in figure 2(a) after $(q+1)$ times of iteration is obtained from a two-step calculation. First, the pressure value $\tilde{p}_n^{(q+1/2)}$ is calculated by averaging the pressure values computed from each of the total N_n integration paths connecting to the current boundary point (s_n) from any of the other boundary points (denoted by s_l) as shown in equation (6):

$$\tilde{p}_n^{(q+1/2)} = \frac{1}{N_n} \sum_{l=1}^{M} \left[R(l,n) \left(\tilde{p}_l^q + \int_{s_l}^{s_n} \nabla \tilde{p} \cdot \boldsymbol{ds} \right) \right] \qquad (6)$$

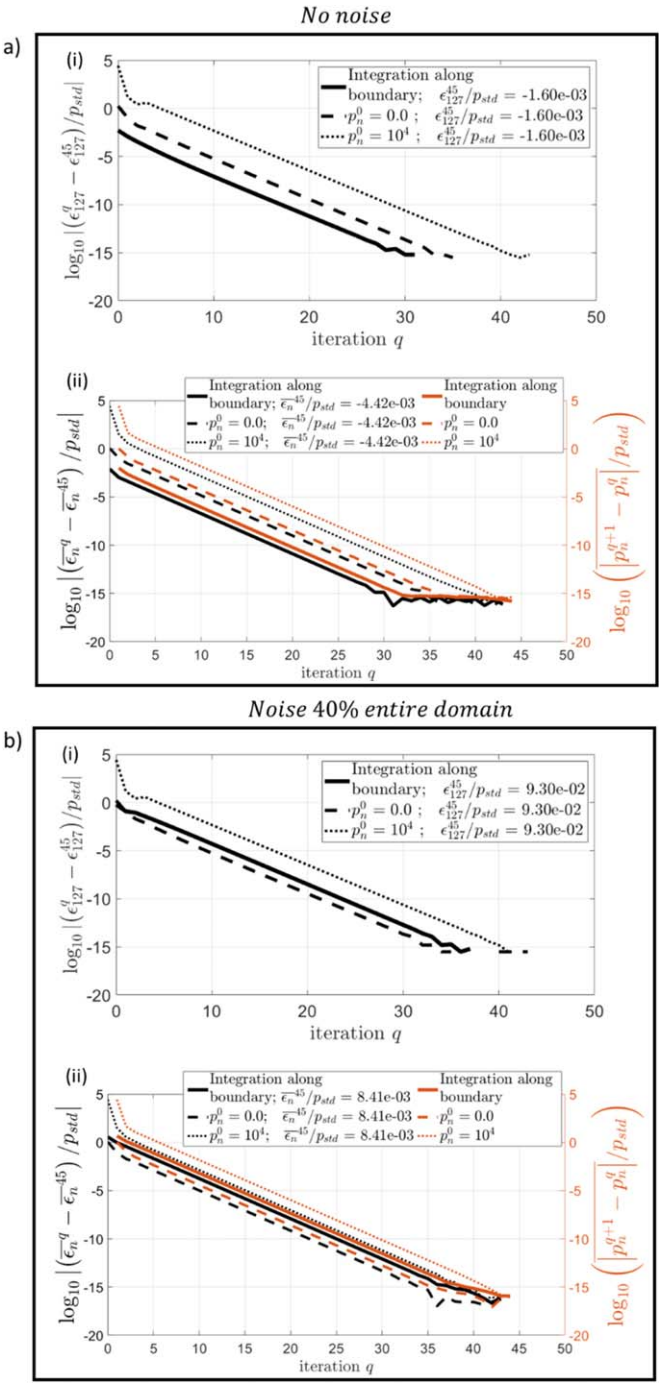

Figure 3. Pressure error convergence at boundary points with three different initial conditions for pressure reconstruction using the parallel ray omnidirectional integration. The pressure error converges to the same value for all initial conditions tested. (a-i) A sample pressure error at the boundary point $(i = 1, j = 127)$, and (a-ii) the average pressure error over all the boundary points reconstructed from the pressure gradient field without embedded noise. (b-i) A sample pressure error at the boundary point $(i = 1, j = 127)$, and (b-ii) the average pressure error over all the boundary points reconstructed from the pressure gradient field embedded with random noise with an amplitude of 40% of $\left(|\nabla p|_{DNS}\right)_{max}$.

where $n = 1\,to\,M$, with M being the total number of the boundary points over the entire computation domain, $R(l,n)$ being the number of repetitive integration path connections

$(R(l,n) \geqslant 1)$ between boundary points (s_l) and (s_n) and $\tilde{p}_l^q$ being the pressure at point s_l obtained after the completion of iteration q. The way that the boundary points connect to each other depends on the type of omnidirectional algorithm used in the pressure reconstruction. In equation (6), $R(l,n)$ and N_n satisfy the following relationship:

$$N_n = \sum_{l=1}^{M} R(l,n). \tag{7}$$

Please note that the second term in equation (6), $\int_{s_l}^{s_n} \nabla\tilde{p} \cdot \boldsymbol{ds}$, which represents the line integration of the measured pressure gradient across the domain between boundary points (s_l) and (s_n), is a fixed value that does not change between iterations. This property was noted in Liu and Katz [7], and has also been utilized ever since by calculating the integral only once during the boundary pressure iteration process when the omnidirectional integration methods are implemented. In this way, redundant calculations can be significantly reduced.

As the second step for calculating pressure $\tilde{p}_n^{(q+1)}$, each time after the completion of one round of iteration within which all boundary points are updated according to equation (6), we apply a correction term to ensure the pressure at the reference point $\tilde{p}_r^{(q+1)}$ is maintained at the fixed reference value $\tilde{p}_{ref}$. The amount of such correction is

$$\Delta_{ref}^{(q+1/2)} = \tilde{p}_{ref} - \tilde{p}_r^{(q+1/2)}. \tag{8}$$

Applying the above correction, we have

$$\tilde{p}_n^{(q+1)} = \tilde{p}_n^{(q+1/2)} + \Delta_{ref}^{(q+1/2)}. \tag{9}$$

In this way, the base error $\left|\Delta_{ref}^{(q+1/2)}\right|$ can be shed off at the end of each round of iteration. Please note that for the omnidirectional integration methods investigated in this paper, the procedures for updating the boundary pressure value $\tilde{p}_n$ are the same.

Note also that the reference pressure $\tilde{p}_{ref}$ may contain an associated error ε_{ref}. For a given pressure gradient field realization, the error ε_{ref} has a fixed value for a given realization of $\tilde{p}_{ref}$:

$$\tilde{p}_{ref} = p_r + \varepsilon_{ref} \tag{10}$$

where p_r denotes the exact pressure value at the reference boundary point s_r. Consistent with this notation, if the exact pressure at a boundary point s_n is p_n, the error ε_n^q at this boundary point after q times of iteration is

$$\varepsilon_n^q = \tilde{p}_n^q - p_n. \tag{11}$$

We can show (see appendix A for details) that the pressure error at a boundary point after each round of iteration contains three parts, as listed below:

$$\varepsilon_n^{(q+1)} = \varepsilon_{nB}^q + \varepsilon_{nA} + \varepsilon_{ref} \tag{12}$$

In equation (12), ε_{nA}, denoting the error accumulated along the integration paths involved in the pressure reconstruction over the flow field domain, can be expressed as

$$\varepsilon_{nA} = \sum_{l=1}^{M} \left[\frac{R(l,n)}{N_n} \left(\varepsilon_{t_{(l,n)}} + \int_{s_l}^{s_n} \varepsilon_{\nabla p} \cdot \boldsymbol{ds} \right) - \frac{R(l,r)}{N_r} \left(\varepsilon_{t_{(l,r)}} + \int_{s_l}^{s_r} \varepsilon_{\nabla p} \cdot \boldsymbol{ds} \right) \right] \tag{13}$$

where N_n and N_r, following the definition in equation (7), represent the total number of integration paths involved in the integration for pressure $\tilde{p}_n$ and $\tilde{p}_r$, respectively. $\varepsilon_{t_{(l,n)}}$ denotes the numerical truncation error for the pressure integration along the path connecting boundary points s_l and s_n, and $\varepsilon_{t_{(l,r)}}$ the numerical truncation error for the pressure integration along the path connecting boundary points s_l and s_r (see figure 2(a)). Because the integration paths that lead to the pressure reconstruction at a certain boundary point (e.g. s_n or s_r) are fixed, the truncation errors $\varepsilon_{t_{(l,n)}}$ and $\varepsilon_{t_{(l,r)}}$, as well as N_n and N_r, are therefore also fixed for a given omnidirectional integration method. In addition, for a given pressure gradient field, $\varepsilon_{\nabla p}$ is also fixed. Consequently, according to equation (13), ε_{nA} is a fixed value which is independent of the number of iterations at the given boundary point location s_n. This observation can be confirmed from figure 8, which will be shown later on in section 4.3.

In equation (12), ε_{nB}^q represents the weighted contribution to $\varepsilon_n^{(q+1)}$ from the pressure errors at all boundary nodal points (ε_l^q, with $l = 1, \ldots, M$) at iteration round q during the calculation of $\tilde{p}_n^{q+1}$. The expression for ε_{nB}^q is defined as

$$\varepsilon_{\mathrm{nB}}^q = \sum_{l=1}^{M} \left\{ \left(\frac{R(l,n)}{N_n} - \frac{R(l,r)}{N_r} \right) \varepsilon_l^q \right\} \tag{14}$$

which can also be written as

$$\varepsilon_{\mathrm{nB}}^q = \sum_{l=1}^{M} \left(w(l,n) \cdot \varepsilon_l^q \right) \tag{15}$$

with $w(l,n)$ denoting a weight that applies to ε_l^q:

$$w(l,n) = \frac{R(l,n)}{N_n} - \frac{R(l,r)}{N_r}. \tag{16}$$

Please note that r in equations (14) and (16) is a fixed number for a given omnidirectional integration calculation. The weight $w(l,n)$ depends only on the omnidirectional integration method used. It is a function of the integration paths involved in the calculation of $\tilde{p}_n^{q+1/2}$ and $\tilde{p}_r^{q+1/2}$, but the value of $w(l,n)$ does not change with the number of iteration q, nor does it change with the pressure gradient field that it is applied to. For a measurement domain with a sufficiently large number of boundary nodal points and a sufficiently dense parallel ray configuration, $|w(l,n)| \ll 1$, $|R(l,n)/N_n| \ll 1$ and $|R(l,r)/N_r| \ll 1$ as shown in figure 4, which presents the distributions of the $w(l,n)$ value and its corresponding component terms $R(l,n)/N_n$ and $R(l,r)/N_r$ over the space

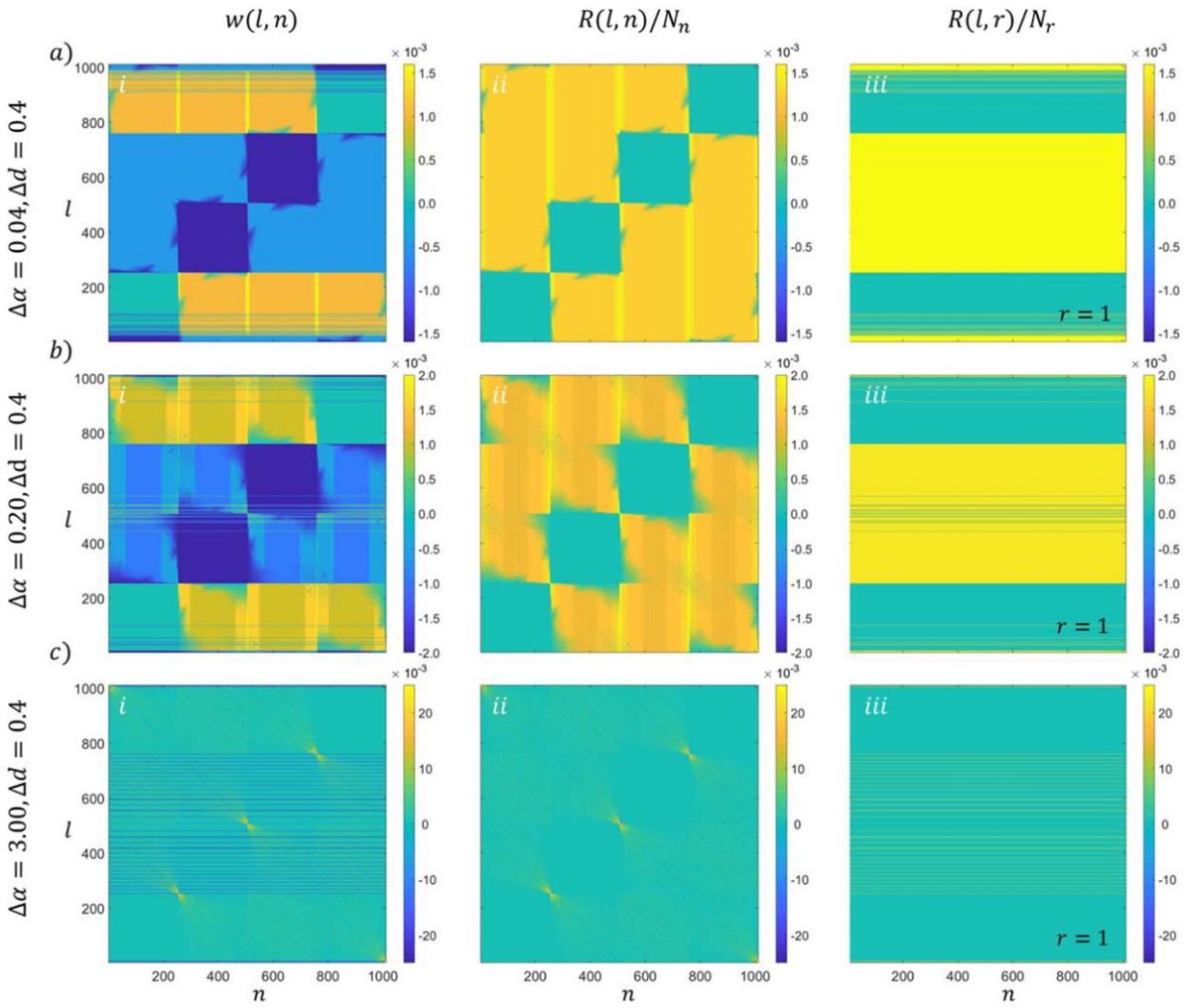

Figure 4. The weight matrix $w(l,n)$ and the corresponding component terms $R(l,n)/N_n$ and $R(l,r)/N_r$ for the rotating parallel ray omnidirectional integration algorithm applied to a 254×254 domain of pressure gradient field, with the reference boundary pressure point selected as the lower-left corner of the domain, thus r = 1. The upper row corresponds to the parallel ray configurations of $(\Delta\alpha = 0.04^\circ, \Delta d^* = 0.4)$, the center row $(\Delta\alpha = 0.20^\circ, \Delta d^* = 0.4)$, and the bottom row $(\Delta\alpha = 3.00^\circ, \Delta d^* = 0.4)$.

of $l-n$ for the rotating parallel ray omnidirectional integration algorithm applied to a 254×254 domain of pressure gradient field. Please note r = 1 in these plots because the reference boundary pressure point is selected as the upper-left corner of the pressure gradient domain. Further comparison in figure 4 indicates that the actual value of $w(l,n)$ depends on the ray density $(\Delta\alpha, \Delta d^*)$, with $\Delta d^* = \Delta d/\Delta h$, where Δh is the grid cell size. For example, for a parallel ray integration with sufficient dense ray configuration, i.e. $(\Delta\alpha = 0.20^\circ, \Delta d^* = 0.4)$, or $(\Delta\alpha = 0.04^\circ, \Delta d^* = 0.4)$, the weight magnitude $w(l,n)$ and its contributing component terms $R(l,n)/N_n$ and $R(l,r)/N_r$, are all on the order of $O\left(10^{-3}\right)$. However, when the ray has a less dense configuration, e.g. $(\Delta\alpha = 3.00^\circ, \Delta d^* = 0.4)$, the values of these coefficients are increased to $O\left(10^{-2}\right)$ as shown in figure 4, implying a reduced rate of convergence. As shown later on in the discussion of section 4.4, the ray density $(\Delta\alpha, \Delta d^*)$ not only influences the rate of convergence for the boundary pressure values, but also affects the reconstructed pressure accuracy. Consistent with the preliminary parameter optimization study by Liu *et al* [15], regarding the optimum choices of line spacing Δd^* and line rotation angle increment $\Delta\alpha$, higher reconstructed pressure accuracy can be achieved by using a denser parallel ray setting. Actually, as revealed by equations (14) and (15), a denser parallel ray setting means more boundary pressure point are connecting to each other. For a fixed boundary point (s_n), to ensure every boundary nodal point (s_l) has at least one chance to connect point (s_n), simple trigonometric analyses by considering the extreme corner point cases require $\Delta\alpha = 0.11^\circ$ and $0.35 < \Delta d^* < 0.71$ for a domain size of 254×254 grids (See appendix B for details).

It can be shown based on linear recurrence theory (see the appendix A for details) that the implicit recursive relationship for the pressure error at the domain boundary as shown in equation (12) can be written as

$$\varepsilon_n^q = \lambda_{n,max}^q C_{n,max} + \varepsilon_{nA} + \varepsilon_{ref} \tag{17}$$

where $C_{n,max}$ is a constant that depends on the pressure initialization (when $q = 0$) at the boundary points and $\lambda_{n,max}$ is the

characteristic error decay rate with its absolute value less than 1, i.e. $|\lambda_{n,max}| < 1$, which means that the boundary pressure error ε_n^q follows an exponential decay with the number of iteration q. Please note that the actual value of $\lambda_{n,max}$ depends on the types of omnidirectional integration algorithm used, and $|\lambda_{n,max}| < 1$ is a characteristic property of the omnidirectional integration methods due to the fact that $|w(l,n)| \ll 1$ as shown in figure 4. As an example, the absolute value of $\lambda_{n,max}$ for the rotating parallel ray omnidirectional integration methods is shown in the appendix A.

Because the characteristic error decay rate $|\lambda_{n,max}| < 1$, after sufficient amount of iterations, according to equation (17), the final boundary pressure error ε_n^q converges to

$$\varepsilon_n^{q_{end}} \approx \varepsilon_{nA} + \varepsilon_{ref}. \tag{18}$$

Equation (18) implies that, according to equation (12):

$$\varepsilon_{nB}^{q_{end}} \approx 0 \tag{19}$$

which is demonstrated in section 4.3 using data from a DNS isotropic turbulence database embedded with imposed errors as testing cases.

3.2. Pressure error at inner nodal points

After the boundary values are converged, pressure values at the inner nodal points can then be calculated using the omnidirectional integration method. As shown in figure 2(b), similar to the calculation of the pressure values at the boundary points, the pressure $\tilde{p}_{ijk}$ at an inner nodal point s_{ijk} is related to a boundary pressure value $\tilde{p}_l$ through an integration path that connects boundary point s_l to point s_{ijk}. In a similar fashion as that for the boundary points, the pressure at an inner nodal point is determined by taking the average of the pressure values obtained along all integration paths coming from all boundary points towards that inner nodal point:

$$\tilde{p}_{ijk} = \frac{1}{N_{ijk}} \sum_{l=1}^{M} \left[R(l,ijk) \left(\tilde{p}_l + \int_{s_l}^{s_{ijk}} \nabla \tilde{p} \cdot \boldsymbol{ds} \right) \right] \tag{20}$$

where N_{ijk} denotes the total number of integration paths that originate from boundary point s_l and pass by the inner nodal point s_{ijk}. Similar to that defined in equation (7):

$$N_{ijk} = \sum_{l=1}^{M} R(l,ijk) \tag{21}$$

where $R(l,ijk)$ represents the number of repetitive connections between points s_l and s_{ijk}. Decomposing the pressure and pressure gradient terms in equation (20) into exact terms and error components according to equations (5) and (11), we have

$$p_{ijk} + \varepsilon_{ijk} = \frac{1}{N_{ijk}} \sum_{l=1}^{M} \left[R(l,ijk) \times \left(p_l + \varepsilon_l + \int_{s_l}^{s_{ijk}} \nabla p \cdot \boldsymbol{ds} + \int_{s_l}^{s_{ijk}} \varepsilon_{\nabla p} \cdot \boldsymbol{ds} \right) \right] \tag{22}$$

where ε_{ijk} is the pressure error at an inner nodal point s_{ijk}, and ε_l is the pressure error at a boundary point s_l after the convergence of the boundary pressure value calculation.

Equation (22) can be simplified by recognizing that the pressure p_l at a boundary point s_l, plus the integral of the exact pressure gradient ∇p along the integration path connecting the boundary point s_l and the inner nodal point s_{ijk}, is equal to the exact pressure p_{ijk} at the inner nodal point s_{ijk} plus the associated truncation error $\varepsilon_{t_{(l,ijk)}}$ due to the numerical method used in the integration along the path:

$$p_l + \int_{s_l}^{s_{ijk}} \nabla p \cdot \boldsymbol{ds} = p_{ijk} + \varepsilon_{t_{(l,ijk)}}. \tag{23}$$

Combining equations (22) and (23), we have

$$\varepsilon_{ijk} = \frac{1}{N_{ijk}} \sum_{l=1}^{M} \left[R(l,ijk) \left(\varepsilon_l + \varepsilon_{t_{(l,ijk)}} + \int_{s_l}^{s_{ijk}} \varepsilon_{\nabla p} \cdot \boldsymbol{ds} \right) \right]. \tag{24}$$

Equation (24) shows that the pressure error at an inner nodal point is the average over all the number of integration paths N_{ijk} for the combination of the pressure error (ε_l) at boundary point s_l, the truncation error $\left(\varepsilon_{t_{(l,ijk)}}\right)$ along the path from boundary point s_l to inner nodal point s_{ijk}, and the line integration of the error embedded in the pressure gradient $\varepsilon_{\nabla p}$ along the path from s_l to s_{ijk}.

After the convergence of the boundary pressure iteration, according to equation (18):

$$\varepsilon_l \approx \varepsilon_{lA} + \varepsilon_{ref}. \tag{25}$$

Plugging equation (25) into equation (24), we have

$$\varepsilon_{ijk} = \frac{1}{N_{ijk}} \sum_{l=1}^{M} \left[R(l,ijk) \left(\varepsilon_{lA} + \varepsilon_{t_{(l,ijk)}} + \int_{s_l}^{s_{ijk}} \varepsilon_{\nabla p} \cdot \boldsymbol{ds} \right) \right] + \varepsilon_{ref} \tag{26}$$

where ε_{lA}, by following the definition in equation (13), is

$$\varepsilon_{lA} = \sum_{m=1}^{M} \left[\frac{R(m,l)}{N_l} \left(\varepsilon_{t_{(m,l)}} + \int_{s_m}^{s_l} \varepsilon_{\nabla p} \cdot \boldsymbol{ds} \right) - \frac{R(m,r)}{N_r} \left(\varepsilon_{t_{(m,r)}} + \int_{s_m}^{s_r} \varepsilon_{\nabla p} \cdot \boldsymbol{ds} \right) \right] \tag{27}$$

As indicated in equations (26) and (27), the final pressure error at an inner nodal point is a function of the weighted average of (i) the line integration of the embedded pressure gradient error over the measurement domain and (ii) the truncation error associated with the numerical line integration, plus (iii) the reference pressure error. Since the weights $|R(l,ijk)/N_{ijk}| \ll 1$, $|R(m,l)/N_l| \ll 1$ and $|R(m,r)/N_r| \ll 1$ (further discussion can be found in section 3.1 with regard to figure 4), as long as the truncation errors and pressure gradient errors are random and homogeneously distributed, both ε_{lA} and ε_{ijk} should be small finite values.

Please note that the error propagation analysis developed in a 3D space is readily applicable to the case of a 2D plane, which is simply a special case of the 3D space with $k = 1$.

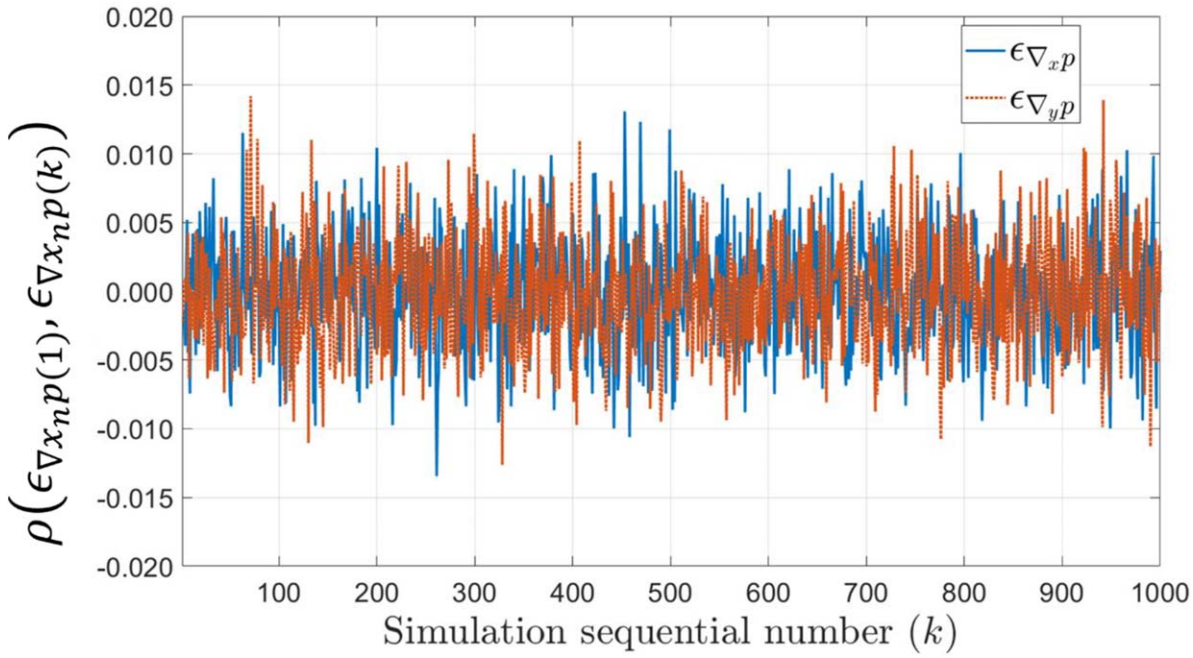

Figure 5. Correlation coefficient between the random pressure gradient noise added to simulation realization 1 and the random pressure gradient noise added to all the subsequent simulation realizations. The near zero correlation coefficient indicates that the pressure gradient noise are uncorrelated.

Thus, for simplicity, in the following section we use a 2D pressure field embedded with homogeneously distributed random error for the verification of the above error propagation analysis.

4. Results

4.1. DNS based test cases

To validate the error propagation model for the omnidirectional integration, we utilize homogeneous isotropic turbulence flow direct numerical simulation (DNS) data available to the public from the John Hopkins University Turbulence Database (JHTDB). The Taylor-scale Reynolds number of this isotropic turbulence flow is 433. Details about the isotropic turbulence database can be found in Perlman *et al* [54], Li *et al* [55], and Graham *et al* [56]. From the database, we select a sample plane containing 256 × 256 grid nodal points. At each of these nodal points, the exact pressure value, as well as the pressure gradient components $\frac{dp}{dx}$ and $\frac{dp}{dy}$ obtained using central finite difference, are available. To simulate the measurement uncertainties, 1000 statistically independent random noise with standard uniform spatial distributions and zero mean value are embedded in the pressure gradient, creating 1000 sample realizations of pressure gradient distribution for the pressure reconstruction error investigation. The random noise is generated using a built-in Matlab® function 'rand', with 1000 distinct seed numbers. The noise amplitude is set to 40% of $\left(|\nabla p|_{DNS}\right)_{max}$, i.e. the maximum magnitude of the pressure gradient in the sample DNS planar data. Figure 5 shows the correlation coefficients (ρ) between the noise embedded in the first simulation map and those in all other simulations. The correlation coefficient ρ is defined as

$$\rho(A,B) = \frac{1}{I_{max}J_{max}-1}\sum_{i=1}^{I_{max}}\sum_{j=1}^{J_{max}}\left[\left(\frac{A_{ij}-\mu_A}{\sigma_A}\right)\left(\frac{B_{ij}-\mu_B}{\sigma_B}\right)\right] \tag{28}$$

where A and B represent the noise added to the pressure gradient components at realizations 1 and k, i.e. $\varepsilon_{\nabla_{x_n}p(1)}$ and $\varepsilon_{\nabla_{x_n}p(k)}$, respectively, with $n = 1$ or 2 corresponding to x or y, and $k = 2$–1000; μ_A and μ_B being the mean values while σ_A and σ_B being the standard deviations of A and B, respectively; and I_{max} and J_{max} being the maximum mesh indices in x and y directions, respectively. The almost zero correlation values ($-0.014 \leqslant \rho \leqslant 0.014$) shown in figure 5 clearly indicate that the random noise distributions superimposed on the DNS pressure gradient field are indeed uncorrelated, i.e. statistically independent.

In PIV velocity measurements, errors in adjacent velocity vectors are correlated. Also, errors can be unevenly distributed due to gaps in the flow seeding and localized regions of elevated shear and rotation. To approximate the error distribution in a more realistic fashion, in addition to the test case of allocating homogeneously distributed random noise with amplitude of 40% of $\left(|\nabla p|_{DNS}\right)_{max}$ to the entire domain of the DNS pressure gradient field (Case A), we also examined three more test cases with 1000 independent realizations each, namely Case B, uniform random noise with amplitude of 40% of $\left(|\nabla p|_{DNS}\right)_{max}$ allocated to a central stripe region in a domain with zero background noise added elsewhere; Case C, uniform random noise with amplitude of 40% of $\left(|\nabla p|_{DNS}\right)_{max}$ allocated to a central stripe region and

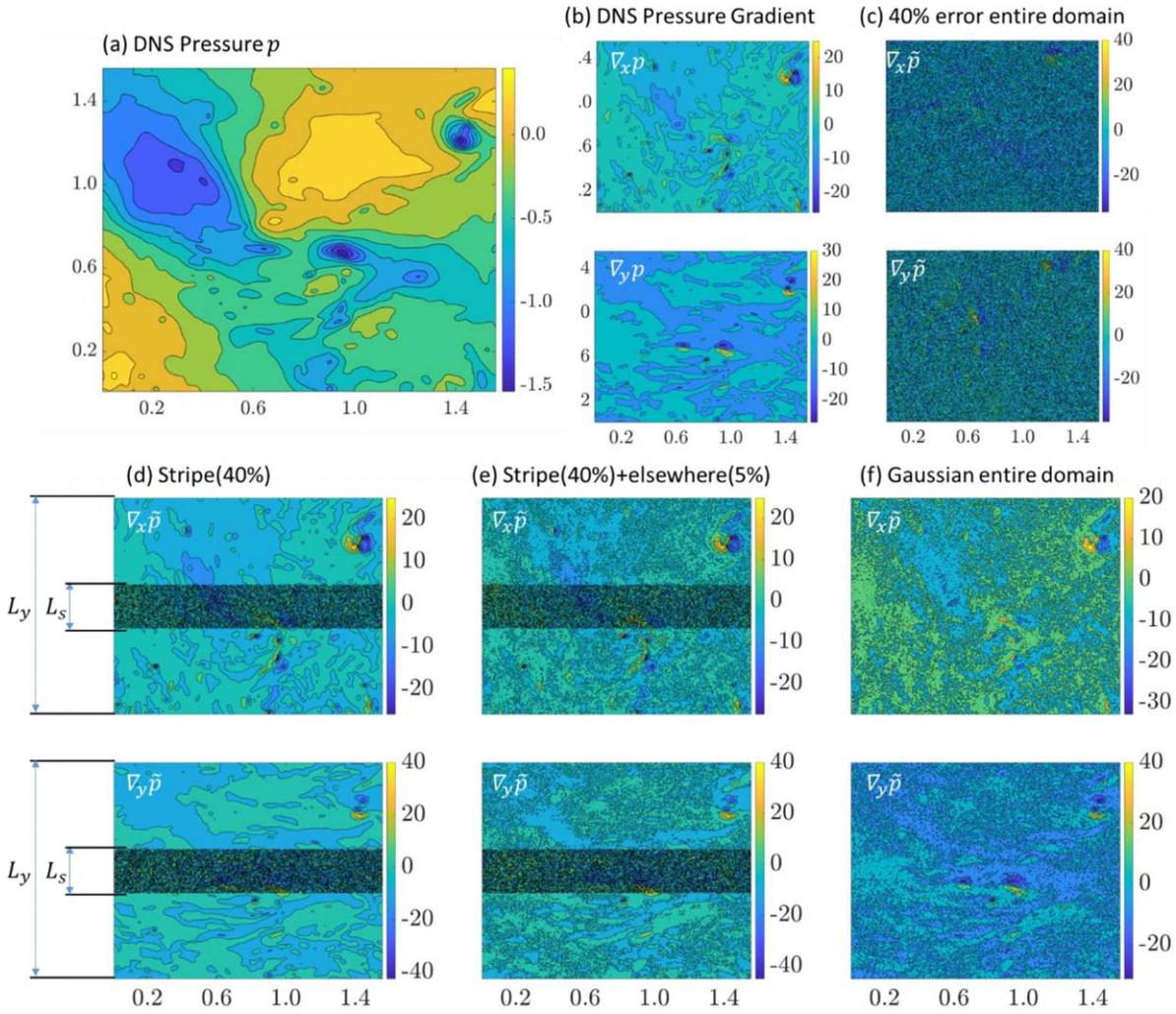

Figure 6. (a) The exact pressure distribution sampled from an isotropic turbulence DNS database. (b) Pressure gradient obtained from the DNS pressure field by central finite difference method. (c) Sample realization (among 1000 of similar ones) of pressure gradient components embedded with random noise with an amplitude of 40% of $\left(|\nabla p|_{DNS}\right)_{max}$, i.e. the maximum DNS pressure gradient magnitude. (d) Sample realization of pressure gradient component distributions with 40% of $\left(|\nabla p|_{DNS}\right)_{max}$ random noise allocated to the central stripe of the domain ($Ls/Ly = 0.20$) and no noise added to the rest of the domain. (e) Sample realization of pressure gradient component distributions with 40% of $\left(|\nabla p|_{DNS}\right)_{max}$ random noise allocated to the central stripe of the domain ($Ls/Ly = 0.20$) and 5.0% noise added to the rest of the domain. (f) Gaussian noise with zero mean and standard deviation of 8.5% of $\left(|\nabla p|_{DNS}\right)_{max}$ superimposed to the entire domain.

5% $\left(|\nabla p|_{DNS}\right)_{max}$background noise added to the rest of the domain; Case D, a Gaussian noise with a zero mean and a standard deviation of 8.5% of $\left(|\nabla p|_{DNS}\right)_{max}$ allocated to the entire domain. With these four test cases, actual flow field applications such as PIV pressure measurement inside a turbulent wake (corresponding to test Cases A and D) or a free shear layer over a cavity (corresponding to test Cases B and C) can be approximately represented.

As an example to show the level of the imposed noise contamination of the pressure gradient fields, figure 6 presents a side-by-side comparison of the DNS pressure gradient field and sample realizations of the four test cases with various scenarios of embedded noise distribution schemes. The error propagation results from these noise contaminated pressure gradient fields using different pressure reconstruction methods will be presented and discussed in sections 4.4 and 4.5, respectively.

4.2. The influence of the numerical truncation error on the final reconstructed pressure error

A mathematical model for the error propagation from the pressure gradient to the pressure reconstructed using omnidirectional integration is introduced in section 3. As indicated in equation (26), the error for the pressure at each inner node point is the average of the pressure error term ε_{lA} as defined in equation (27), the truncation error $\varepsilon_{t(l,ijk)}$ along the paths linking boundary point s_l to inner nodal point s_{ijk}, and the line integration of the error embedded in the pressure gradient $\varepsilon_{\nabla \mathrm{p}}$ along paths from s_l to s_{ijk}. Since ε_{lA} is only an average of the truncation terms $\varepsilon_{t_{(m,l)}}$ and $\varepsilon_{t_{(m,r)}}$ and the line integration of the pressure gradient error term $\varepsilon_{\nabla p}$ as defined in equation (27), overall ε_{ijk} is only a function of the truncation error terms and the pressure gradient error terms. For the DNS data discussed in section 4.1, since the pressure gradient

components $\frac{dp}{dx}$ and $\frac{dp}{dy}$ are obtained using central difference method, the error term path $\varepsilon_{\nabla \mathrm{p}}$ in equations (26) and (27) can then be further decomposed into two parts, one is $\varepsilon_{\nabla \mathrm{p}_{\mathrm{trunc}}}$ denoting the truncation error due to central difference scheme; the other is $\varepsilon_{\nabla \mathrm{p}_{\mathrm{noise}}}$ denoting the noise superimposed onto the pressure gradient components. When there is no noise added to the pressure gradient, the final error of the reconstructed pressure is only a function of the truncation error terms, i.e. the terms involving $\varepsilon_{t(l,ijk)}$, $\varepsilon_{t_{(m,l)}}$, $\varepsilon_{t_{(m,r)}}$ and $\varepsilon_{\nabla \mathrm{p}_{\mathrm{trunc}}}$, according to equations (26) and (27). For the present study, the line integration is implemented using the trapezoidal method, which has a second order truncation error with respect to grid size ($\sim O\left(h^2\right)$, Gerald and Wheatley [57]). The final pressure error variation with respect to the truncation errors $\varepsilon_{t(l,ijk)}$, $\varepsilon_{t_{(m,l)}}$ and $\varepsilon_{t_{(m,r)}}$ (please note all these three truncation errors are of the same nature) is evaluated by under-sampling the pressure gradient domain (i.e. skipping nodal points to achieve coarse grid) while keeping the domain size constant and using the original pressure gradient values on the coarse grids (the truncation error due to $\varepsilon_{\nabla \mathrm{p}_{\mathrm{trunc}}}$ is fixed in this study). The grid size is defined in nondimensional form as

$$h^* = \frac{\Delta x_k}{\Delta x_{min}} = \frac{N_{max} - 1}{N_k - 1} \tag{29}$$

where Δx_{min} and Δx_k denote the original and the increased grid sizes, respectively, and N_{max} and N_k the number of the total nodal points along the horizontal side (the x-direction) for the original and the under-sampled grids, respectively. The parameters for the grids tested are summarized in table 1. Two sample cases were evaluated: one case with no noise added and one case with 40% noise (with respect to the maximum magnitude of the DNS pressure gradient in the domain) added to the pressure gradient. For both cases, the pressure was reconstructed using the rotating parallel ray omnidirectional integration ($\Delta\alpha = 0.2^0, \Delta d^* = 0.4$). For each grid size, the spatial average of the absolute value of the error normalized by the standard deviation of the exact (DNS) pressure in the domain ($\overline{|\varepsilon_{ij}|}/p_{std}$) is obtained and plotted in logarithmic scale against the nondimensional grid spacing, as shown in figure 7. For the case without added noise, the pressure error increases approximately as a second order power of the grid spacing, indicating the pressure error in this case is indeed in agreement with the trapezoidal truncation error ($\sim O(h^2)$) involved in the pressure reconstruction. In contrast, when the 40% noise is superimposed over the entire domain (Case A), the pressure error increases with the grid size at an approximately first order increasing rate, i.e. approximately in a linear fashion, indicating that the pressure gradient error terms $\int_{s_l}^{s_{ijk}} \varepsilon_{\nabla p} \boldsymbol{ds}$, $\int_{s_m}^{s_l} \varepsilon_{\nabla p} \cdot \boldsymbol{ds}$ and $\int_{s_m}^{s_r} \varepsilon_{\nabla p} \cdot \boldsymbol{ds}$ in equations (26) and (27) have dominant contribution over the truncation error terms to the final pressure error.

4.3. Error convergence for boundary pressure values through iteration

As shown in equations (12) and (15), the convergence of the boundary pressure error $\varepsilon_n^{(q+1)}$ is achieved through the error term ε_{nB}^q, which in turn relies on the weight coefficient matrix $w(l,n)$ that applies to the boundary pressure error ε_l^q to reduce the error. As discussed in section 3.1 and shown in figure 4, $|w(l,n)| \ll 1$ for a sufficiently dense parallel ray configuration, which provides the basis for $\varepsilon_{nB}^{q_{end}} \approx 0$ (i.e. equation 19) and correspondingly ε_l^q eventually reduced to $\varepsilon_n^{q_{end}} \approx \varepsilon_{nA} + \varepsilon_{ref}$ (i.e. equation 18) as discussed in section 3.1. To show this evolution process, figure 8 presents the evolution process of the boundary pressure error convergence for pressure error ε_n^q and error components ε_{nA} and ε_{nB}^q with respect to iteration round q at all boundary points for representative isotropic turbulence test cases with and without the 40% noise added to the entire pressure gradient field. As mentioned in section 3.1, ε_{nA} does not change through iteration. This observation is verified in figure 8 by examining the evolution process of ε_{nA} for both testing cases (i.e. with and without added noise). In contrast, the overall amplitudes for both ε_n^q and ε_{nB}^q are reduced gradually through iteration, with their final values converged to $\varepsilon_n^{q_{end}} \approx \varepsilon_{nA} + \varepsilon_{ref} = \varepsilon_{nA}$ ($\varepsilon_{ref} = 0$ for both cases tested) and $\varepsilon_{nB}^{q_{end}} \approx 0$, respectively, as expected. Please note, the initial error distributions ε_n^0 for both testing cases are the same because for both cases the boundary values are all initialized with zero values at the beginning of the pressure reconstruction.

As shown in equation (13), ε_{nA} is a result of the weighted summation of the truncation errors $\varepsilon_{t_{(l,n)}}$ and of $\varepsilon_{t_{(l,r)}}$ as well as the spatial integration of pressure gradient error $\varepsilon_{\nabla p}$. Since the weights $|R(l,n)/N_n| \ll 1$ and $|R(l,r)/N_r| \ll 1$, as long as the truncation errors and pressure gradient errors are random and homogeneously distributed, the final weighted summation, i.e. ε_{nA} should be a small finite value. This expectation is verified from figure 8 as well.

4.4. Performance of pressure reconstruction methods with test case A, i.e. 40% random pressure gradient noise superimposed over the entire domain

Four different methods are used for pressure reconstruction from the pressure gradient fields embedded with the 40% random noise over the entire domain (i.e. test Case A). One method is the solution of the Poisson equation for pressure using a second order central difference method (similar as Ghaemi *et al* [58]; Ghaemi and Scarano [59]; Villegas and Diez [60]) with Neumann boundary condition for all boundary points except the lower left corner where a fixed reference pressure value ($p_{ref} = \mathrm{P}_{\mathrm{DNS}}(1,1)$) is prescribed. This method is referred to as 'Poisson NBC' in the following discussion. Another variant of the Poisson equation method is 'Poisson $\mathrm{DBC}_{\mathrm{Parallel\ Ray}}$', which uses the pressure values on all boundary points obtained by the rotating parallel ray omnidirectional integration as the Dirichlet boundary conditions. The other two methods are variations of the omnidirectional integration, with the first one being the rotating parallel ray omnidirectional integration method [15], and the second one the circular virtual boundary omnidirectional integration method [10, 12]. Same as the implementation in the Poisson NBC equation approach, the reference pressure during the implementation of the omnidirectional pressure reconstructions is

Table 1. Summary of under-sampled grids for integration truncation error evaluation.

Sampling sequence	Number of grid nodal points ($N_k \times N_k$)	Domain length (L_x)	Domain height (L_y)	Horizontal grid size (Δx)	Vertical grid size (Δy)	Nodimensional grid size (h^*)
1	253 × 253	1.546	1.546	6.14×10^{-3}	6.14×10^{-3}	1.00
2	127 × 127	1.546	1.546	1.23×10^{-2}	1.23×10^{-2}	2.00
3	85 × 85	1.546	1.546	1.84×10^{-2}	1.84×10^{-2}	3.00
4	64 × 64	1.546	1.546	2.45×10^{-2}	2.45×10^{-2}	4.00
5	43 × 43	1.546	1.546	3.68×10^{-2}	3.68×10^{-2}	6.00
6	37 × 37	1.546	1.546	4.30×10^{-2}	4.30×10^{-2}	7.00
7	29 × 29	1.546	1.546	5.52×10^{-2}	5.52×10^{-2}	9.00

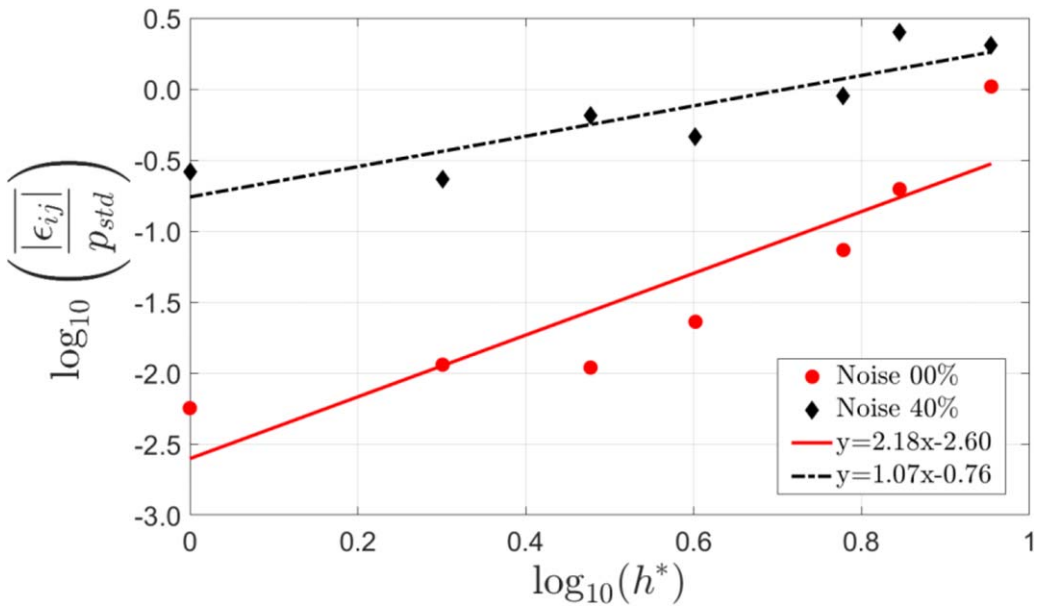

Figure 7. Average of the absolute error normalized by the standard deviation of the DNS isotropic turbulence pressure as a function of the normalized grid size to show the influence of the integration truncation error on the pressure reconstruction accuracy. Without the embedded noise in the pressure gradient, the accuracy of the parallel ray omnidirectional integration is proportional to about the second order of the grid size, i.e. the same order of the trapezoidal method used to perform the line integrations. With noise at an amplitude of 40% of $\left(|\nabla p|_{DNS}\right)_{max}$ embedded in the entire domain, the accuracy is proportional to about the first order of the grid size.

set to be the DNS pressure at the lower left corner of the flow field.

The error in the reconstructed pressure is computed as the difference between the reconstructed pressure and the exact (i.e. DNS) pressure:

$$\varepsilon_{ij} = \tilde{p}_{ij} - p_{ij} \tag{30}$$

with its standard deviation defined as

$$\varepsilon_{std} = \sqrt{\frac{1}{I_{max}J_{max} - 1} \sum_{i=1}^{I_{max}} \sum_{j=1}^{J_{max}} \left(\varepsilon_{ij} - \overline{\varepsilon_{ij}}\right)^2} \tag{31}$$

where (and throughout the paper) the overbar represents the spatial averaging over the entire domain for a specific reconstructed pressure realization (i.e. for a specific instant of time).

Figure 9 presents the cumulative average of the standard deviation error and the maximum and minimum error bounds found for the pressure reconstructed using the aforementioned integration methods. In figure 9, all quantities are normalized by the standard deviation of the DNS pressure p_{std} obtained in the original 256 × 256 sample planar domain. From figure 9(a), it can be seen that there exists a significant difference between the error bounds for the omnidirectional integration methods and that of the Poisson method with Neumann boundary condition (Poisson NBC). For the omnidirectional methods, the errors are always bellow 0.25 while the error for the Poisson NBC exceeds 2.67, about one order of magnitude higher. Also, the average errors for the omnidirectional integration methods are below 0.17 and the average error for Poisson NBC is about 0.86. To further discern the performance difference between the two omnidirectional integration methods investigated, a zoomed-in version of figure 9(a) is shown in figure 9(b), from which the improvement in performance from the circular virtual boundary omnidirectional integration method to the rotating parallel ray omnidirectional integration method can be clearly seen. It is important to note that, as shown in Liu *et al* [15], the performance of the rotating parallel ray depends on the rotation angle increment $\Delta\alpha$ and the distance between rays Δd^* (normalized by the grid spacing). For the isotropic

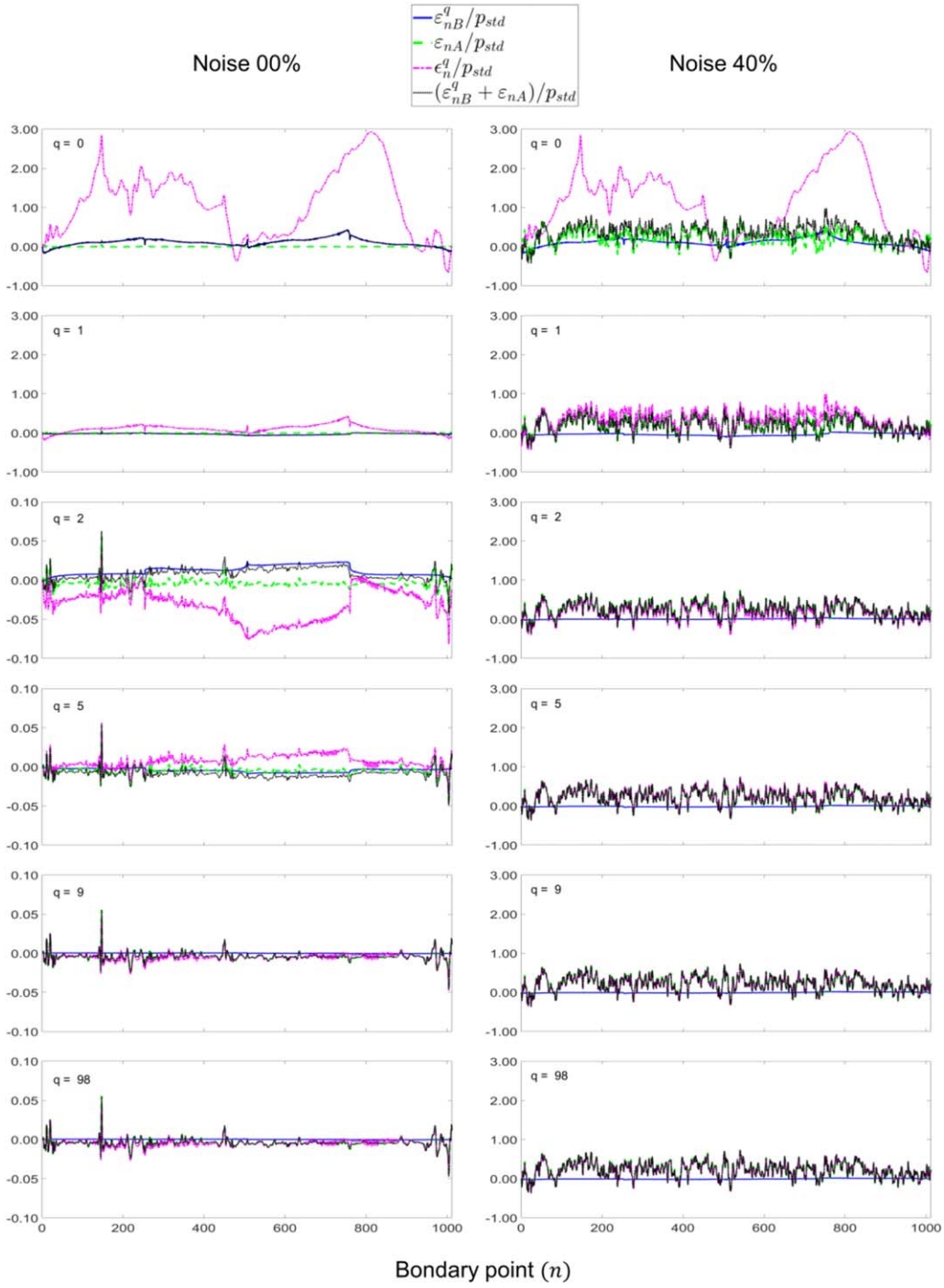

Figure 8. The evolution of the boundary pressure error convergence for the pressure error ε^q_n and the error components ε_{nA}, and ε^q_{nB} at representative iteration rounds. The left column shows the error evolution for the isotropic turbulence test case without noise added. The right column shows the error evolution for the test case with 40% noise added to the entire pressure gradient field (test Case A). For both cases, $\varepsilon_{ref} = 0$. Please note the y-axis scales for $q = 1$ and 2 on the left column are different from the rest plots in that column. Also please note, the initial error distributions ε^1_n for both testing cases are the same because of the zero-boundary value initialization for both cases.

turbulence DNS data investigated in this work, the optimal pressure reconstruction result is obtained when $\Delta d^* = 0.4$ and $\Delta\alpha = 0.2^0$ for the rotating parallel ray pressure reconstruction method.

Figure 9(b) also highlights the benefit of using the rotating parallel ray omnidirectional integration to generate Dirichlet boundary conditions that are then applied to the Poisson equation for pressure (Poisson $\text{DBC}_{\text{Parallel Ray}}$). It can be seen from figure 9(b) that using the Dirichlet boundary conditions achieved by the optimal parallel ray omnidirectional integration, the Poisson DBC method performs better than the virtual boundary omnidirectional integration method, while it is still slightly outperformed by the optimal parallel ray omnidirectional integration method by 0.2% with respect to p_{std}. For

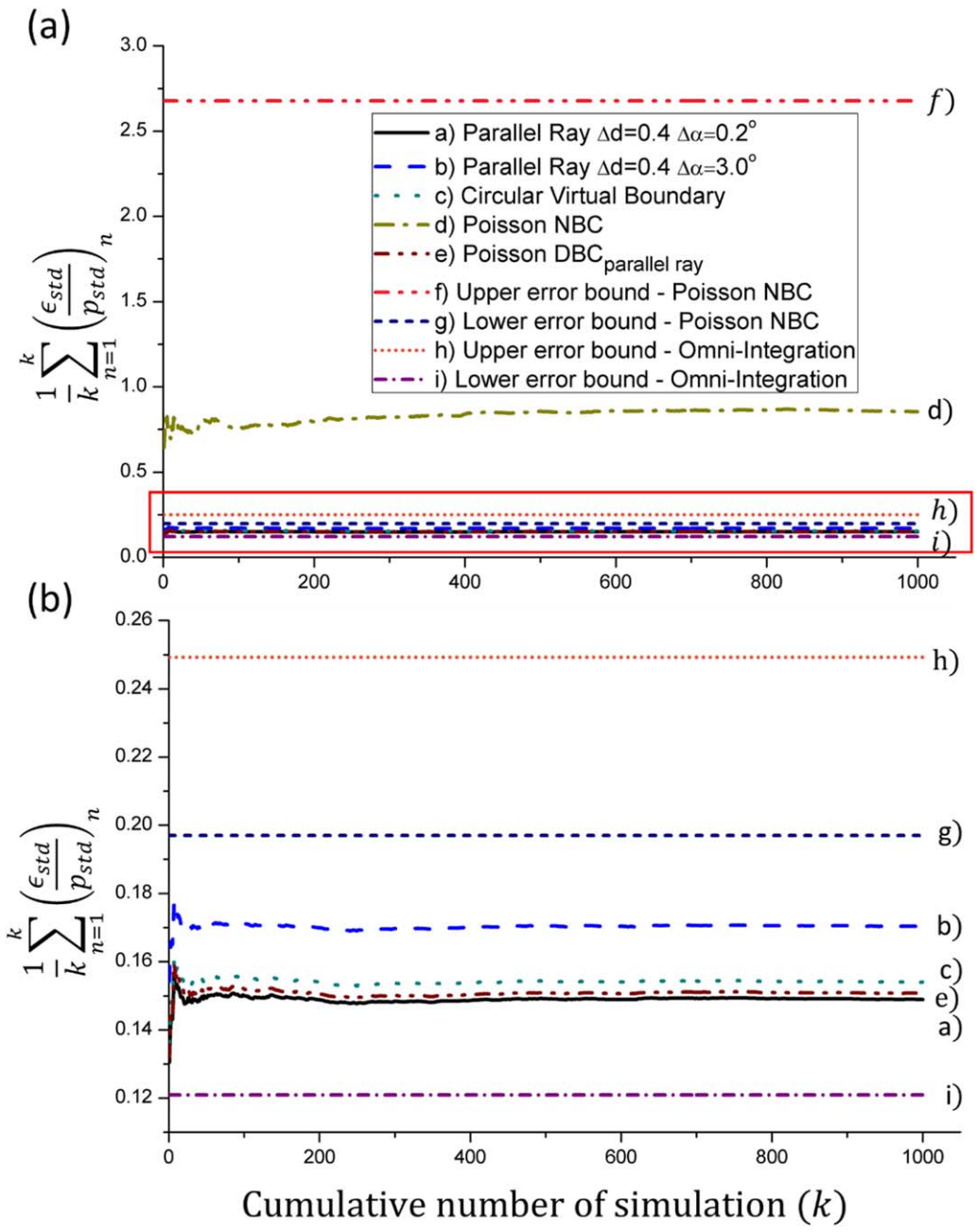

Figure 9. Cumulative average error of the reconstructed pressure for 1000 realizations with noise at an amplitude of 40% of $\left(|\nabla p|_{DNS}\right)_{max}$ superimposed on the entire domain of a sample isotropic turbulence pressure gradient field. Convergence is achieved after 500 simulations for the Poisson equation method with the Neumann boundary condition (Poisson NBC). For the omnidirectional methods, the error convergence is achieved after about 100 simulations. (a) Comparison of the cumulative average error for the pressure reconstruction methods tested; (b) zoomed-in plot showing the details of the comparison among the methods tested.

many experimental applications it is not possible to obtain the pressure at the domain boundaries to prescribe the Dirichlet boundary condition. Pan *et al* [45], summarizes 16 applications of the Poisson method for the pressure measurement in PIV experiments; only one uses Dirichlet boundary condition [61], two make use of Neumann boundary condition [60, 62] and the others use mixed boundary conditions [21, 27, 36, etc]. To overcome this limitation, one can use the omnidirectional integration to obtain the pressure at the boundary points and then prescribe it as Dirichlet boundary conditions to the Poisson equation solver for pressure reconstruction over the rest of the domain.

The simulation results support the theoretical analysis presented in section 3. The propagated random error from the pressure gradient to the reconstructed pressure is significantly lower for the omnidirectional methods in comparison with the Poisson NBC approach. Table 2 summarizes the average error, the standard deviation of the error and the maximum error for the 1000 pressure field realizations reconstructed from the corresponding pressure gradient field of a DNS of isotropic

Table 2. Average error and error standard deviation for 1000 pressure reconstruction realizations from the DNS isotropic turbulence pressure gradient field embedded with random noise over the entire domain with an amplitude of 40% of $\left(|\nabla p|_{DNS}\right)_{max}$.

Method	$\frac{1}{1000}\sum_{n=1}^{1000}\left(\frac{\varepsilon_{std}}{p_{std}}\right)_n$	$\left(\frac{\varepsilon_{std}}{p_{std}}\right)_{std}$	$\left(\frac{\varepsilon_{std}}{p_{std}}\right)_{max}$
Rotating parallel ray $\Delta d^* = 0.4$, $\Delta\alpha = 0.2^\circ$	0.149	0.015	0.231
Rotating parallel ray $\Delta d^* = 0.4$, $\Delta\alpha = 3.0^\circ$	0.170	0.014	0.249
Circular virtual boundary integration	0.154	0.015	0.232
Poisson equation $\text{DBC}_{\text{parallel ray}}$	0.151	0.015	0.230
Poisson equation NBC	0.854	0.406	2.678

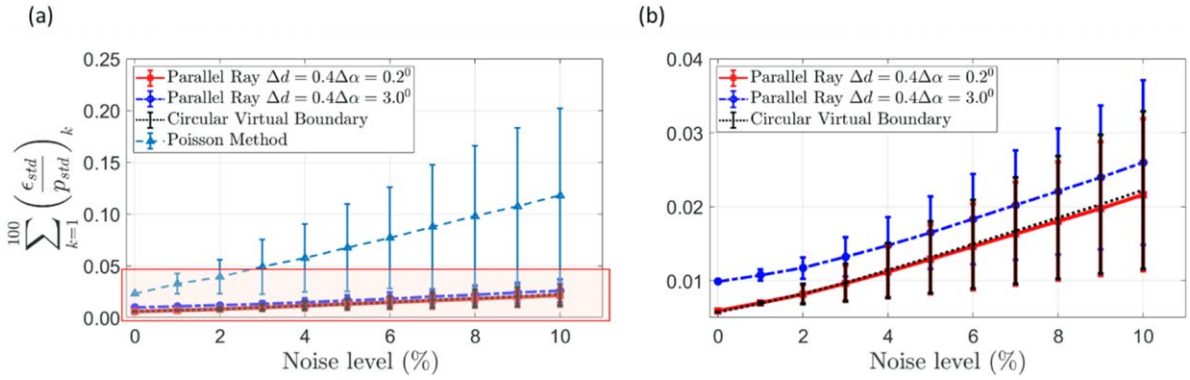

Figure 10. Comparison of pressure reconstruction error with respect to random noise levels from 1% to 10% added to the pressure gradient field. At each noise level, 100 uncorrelated noise distributions are used to compute the average error and the standard deviation. The average error and the standard deviation of the error increase as the noise level increases for all methods, however it is clear that the omnidirectional integration is less affected by the noise than the Poisson equation method with Neumann boundary conditions. (a) Result for Poisson NBC and omnidirectional integration methods; (b) zoomed-in plot showing the pressure error of the omnidirectional integration methods.

turbulence with embedded random noise. As can be seen from table 2, the error for the Poisson NBC approach is one order of magnitude higher than the omnidirectional methods.

To investigate the effect of the noise level on the accuracy of the pressure reconstruction methods, we evaluate the error propagation from the pressure gradient fields with added random noise at amplitudes varying from 1% to 10% of the maximum magnitude of the DNS pressure gradient, i.e. a relative noise level range close to that can be seen in actual experiments [10]. A total of 100 statistically independent random noise distributions are generated for each noise level investigated using distinct seed numbers. The pressure is then reconstructed and compared with the exact pressure. The average pressure errors over the 100 realizations $\overline{\varepsilon_{std}} = \frac{1}{100}\sum_{n=1}^{100}\left(\frac{\varepsilon_{std}}{p_{std}}\right)_n$ varying with the added noise level for different reconstruction methods are shown in figure 10. The error bars shown in this figure represent the $\pm 1.0\sigma$ ranges of the quantity ε_{std}. It can be seen that the average pressure error and its standard deviation using Poisson NBC approach are much larger than those of the omnidirectional integration methods for all noise intensities simulated. As shown in figure 10, it can be seen that for all methods tested, the error on the reconstructed pressure increases almost linearly with the noise levels (1%–10%) embedded in the pressure gradient field. This trend is in agreement with Charonko *et al* [34]. When the embedded noise level increases, the magnitude of the pressure reconstruction error also increases, with the pressure error for Poisson NBC approach increasing at a higher rate compared to the omnidirectional approaches.

It is important to note that, as mentioned earlier, the accuracy for the rotating parallel ray omnidirectional integration method depends on the number of rays used, which is governed by the choice in the parameter space $(\Delta\alpha, \Delta d^*)$. As shown in figures 9(b) and 10, a dense parallel ray represented by the parameter values of $\Delta\alpha = 0.2^\circ$ and $\Delta d^* = 0.4$ is more favorable in providing pressure reconstructed result with higher accuracy than the less dense parallel ray as represented by the parameter values of $\Delta\alpha = 3.0^\circ$ and $\Delta d^* = 0.4$. This is in agreement with equation (24) which predict low error for pressure at the inner points with the increase of the number of rays (N_{ijk}). Please note, as shown in Liu *et al* [15], after a certain optimal value, further increase of the parallel ray density may deteriorate the pressure reconstruction accuracy because of the more numerical errors involved in the calculation.

To intuitively understand the effect of the pressure reconstruction performance, figure 11 presents comparisons of the reconstructed pressure $\tilde{p}$, the error of the reconstructed pressure ε_{ij} and the probability density function (PDF) distribution of ε_{ij} obtained by using different pressure reconstruction methods for their corresponding worst (i.e. the largest ε_{std}) and best (i.e. the least ε_{std}) cases of performance among the 1000 pressure field realizations reconstructed from the pressure gradient field with the 40% embedded random error. It can be seen that, for most representative cases, even with the 40% embedded random, the essential features of the original

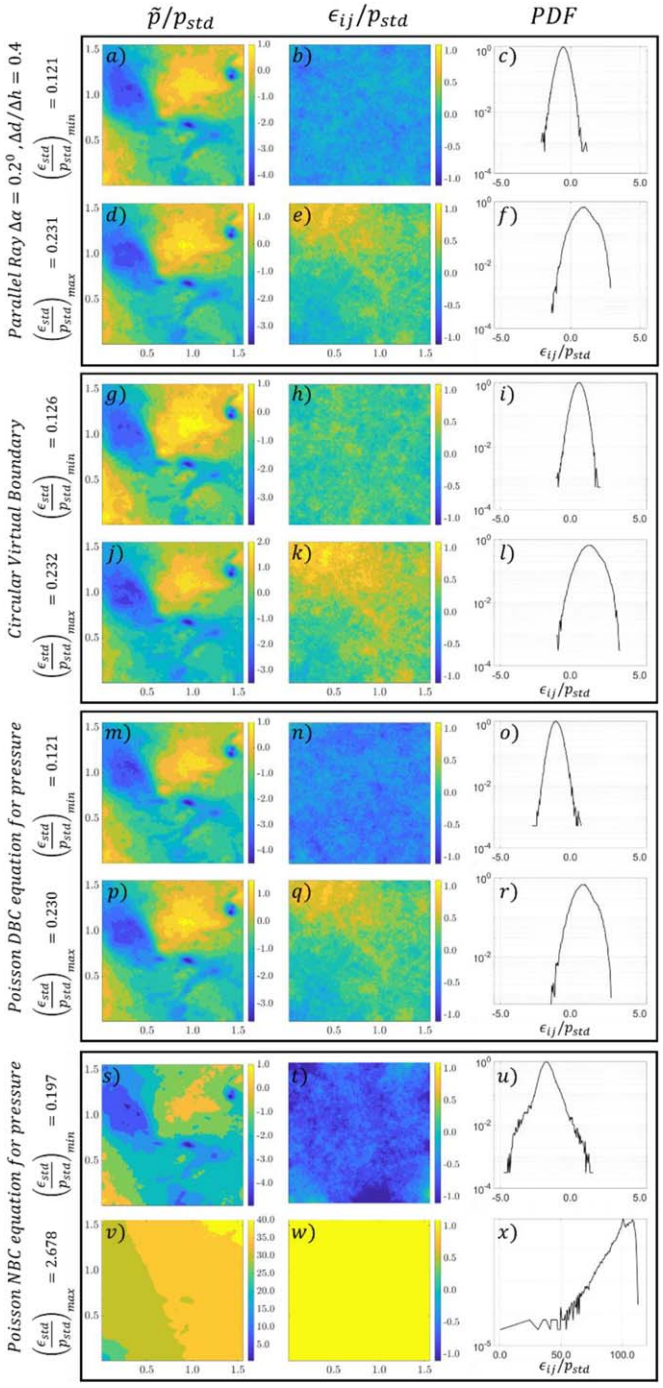

Figure 11. Representative results with the maximum and minimum ε_{std} error distributions based on the 1000 pressure realizations reconstructed using parallel ray omnidirectional integration, circular virtual boundary omnidirectional integration, Poisson equation method with Dirichlet boundary condition (generated by the parallel ray omni-integration) and the Poisson equation method with Neumann boundary condition. Within each case, the first column shows the reconstructed pressure distributions, the second column shows the pressure error distributions, and the last column shows the pressure error probability density function corresponding to each pressure distribution sample.

DNS pressure distribution (as shown in figure 6(a)) can still be successfully captured by most of the pressure reconstruction methods, except the worst case scenario for Poisson NBC (figure 11(v)), where the reconstructed pressure distribution failed in capturing the essential patterns for the original DNS pressure distribution. The pressure error PDF profiles for both the best and worst cases of performance of the three methods (i.e. parallel ray omnidirectional integration, circular virtual boundary omnidirectional integration, Poisson equation method with parallel ray generated Dirichlet boundary condition) are very similar. Consistent with the mean and fluctuation pressure distributions, for both the best and the worst cases, the error range of the Poisson equation method with Neumann boundary condition are much larger (about 2 times larger for the best case, and 30 times larger for the worst case) than those associated with other methods, as shown in the PDF plots in figure 11.

To compare the behaviour of the error propagation in wave number space, as shown in figure 12, we compute the power spectrum density of the reconstructed pressure from the 1000 realizations of the 40% noise embedded isotropic turbulence DNS data using the rotation parallel ray method (RPR, $\Delta d^* = 0.4$, $\Delta\alpha = 0.2^\circ$), and compare it with those using the circular virtual boundary (CVB) omnidirectional method, the Poisson equation with Dirichlet boundary condition based on boundary pressure data provided by RPR ($\Delta d^* = 0.4$, $\Delta\alpha = 0.2^\circ$), the RPR with coarse ray density ($\Delta d^* = 0.4, \Delta\alpha = 3.0^\circ$); and the Poisson equation with Neumann boundary condition, respectively, with the DNS pressure spectrum used as a ground-truth for comparison. Consistent with the discussion regarding figure 9, the rotation parallel ray method with dense ray density (RPR, $\Delta d^* = 0.4, \Delta\alpha = 0.2^\circ$) shows the best performance among the methods compared. The Poisson NBC method has the largest deviation across the entire wavenumber space, especially at the high wavenumber space. When we use the boundary pressure data provided by RPR ($\Delta d^* = 0.4, \Delta\alpha = 0.2^\circ$) as a Dirichlet boundary condition for the Poisson equation method, same power spectrum density distribution with that of RPR ($\Delta d^* = 0.4, \Delta\alpha = 0.2^\circ$) is achieved, as shown in figure 12(b). Overall the reconstructed pressure using omnidirectional integration methods (both RPR and CVB) agree quite well with the DNS pressure spectrum at low wavenumber space. However, considerable deviation from the DNS pressure spectrum occurs at the high wave number space, indicating for most part, the error propagation for the omnidirectional methods occur locally. Especially, when coarse ray density ($\Delta d^* = 0.4, \Delta\alpha = 3.0^\circ$) is used, the deviation at high wavenumber space become deteriorated.

4.5. Performance of pressure reconstruction methods with test cases B, C and D

To further investigate the performance of the pressure reconstruction methods, in addition to test case A discussed in section 4.4, we also examined three more test cases B, C, and D based on their corresponding 1000 independent realizations, respectively. The error distributions introduced in these three test cases are described in section 4.1. Performance results in terms of cumulative average error of reconstructed pressure obtained with these three testing cases are summarized in figure 13. As shown from the figure, for all

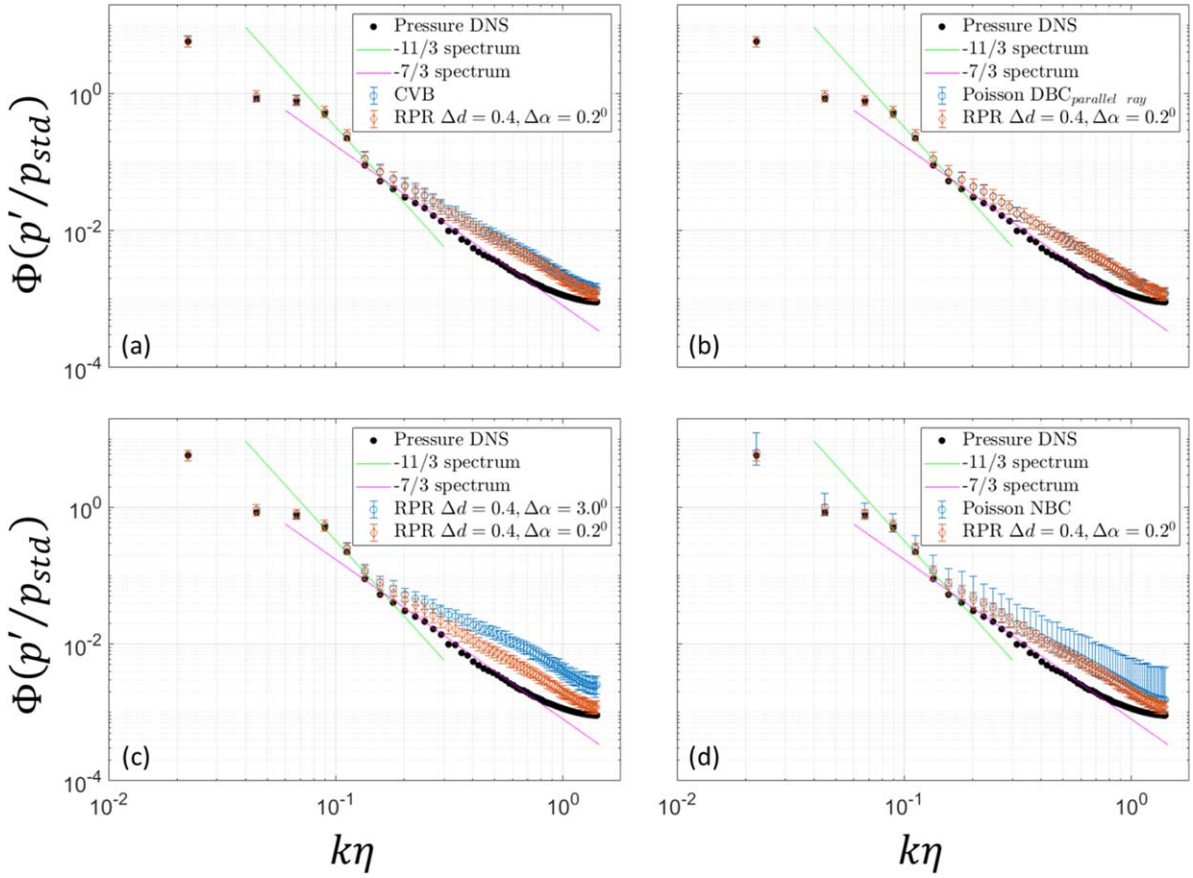

Figure 12. Comparison of the power spectral density of the reconstructed pressure from the 1000 realizations of the 40% noise embedded isotropic turbulence DNS data using the rotation parallel ray method (RPR, $\Delta d/\Delta h = 0.4, \Delta\alpha = 0.2^\circ$) with those using (a), the circular virtual boundary (CVB) omnidirectional method; (b), the Poisson equation with Dirichlet boundary condition (Poisson DBC) based on boundary pressure data provided by RPR ($\Delta d/\Delta h = 0.4, \Delta\alpha = 0.2^\circ$); (c), RPR with coarse ray density ($\Delta d/\Delta h = 0.4, \Delta\alpha = 3.0^\circ$); and (d) the Poisson equation with Neumann boundary condition, respectively. The spectrum of the DNS pressure is used as a ground-truth for comparison.

three test cases, namely, case B, 40% random noise superimposed to the central stripe and no noise added elsewhere in the domain; Case C, 40% random noise superimposed to the central stripe and 5.0% noise added to the rest of the domain; and Case D, Gaussian noise superimposed to the entire domain, the performance ranks for different pressure reconstruction methods are consistent, with the rotation parallel ray omnidirectional integration method ($\Delta d^* = 0.4, \Delta\alpha = 0.2^\circ$) being the practical method of choice with the best pragmatically achievable accuracy in terms of averaged error standard deviation $(\varepsilon_{std}\backslash p_{std})_{avg}$. Poisson equation exhibits almost the same accuracy performance if the boundary pressure values obtained by parallel ray ($\Delta d^* = 0.4, \Delta\alpha = 0.2^\circ$) are used as Dirichlet boundary condition for the Poisson solver. As an ideal test of the performance limit, when the DNS boundary pressure serves as Dirichlet boundary condition (which is not available in practice), the Poisson solver shows the best ideal performance in reconstructed pressure accuracy. However, if the DNS boundary pressure is used to replace the last round of iteration-obtained boundary pressure values for the parallel ray method ($\Delta d^* = 0.4, \Delta\alpha = 0.2^\circ$), the performance is not as good as that of the Poisson DBC (with exact DNS values). The reason for that is for the parallel ray omnidirectional integration (or other omnidirectional approach in general), the boundary pressure values, no matter whether they are obtained from converged iteration, or from the assigned exact DNS values like this test case, provide only a basis for the start values of the last round of omnidirectional integration (mainly for determining the pressure values at the inner nodal points). The boundary points at the end of the integration on solid boundaries are open for receiving new values obtained from the omnidirectional integration. Along with the omnidirectional integration process, an error of ε_{nA} is inevitably generated as indicated in equations (13) and (18), and will be carried to the pressure distributions over the entire domain, including the boundary pressure error as defined in equation (18) and the pressure error at inner nodal points as defined in equations (26) and (27). In contrast, when the DNS pressure serves as the Dirichlet boundary condition for the Poisson solver, the boundary pressure value is set to be rigid and fixed, thus ensuring accurate match on the boundaries, and as a result, rendering the least theoretically achievable error for the reconstructed pressure. This explanation is in agreement with supporting evidence shown in figures 16 and 17, which will be discussed later.

As discussed in section 4.4, a popular practice regarding boundary pressure value prescription for Poisson equation

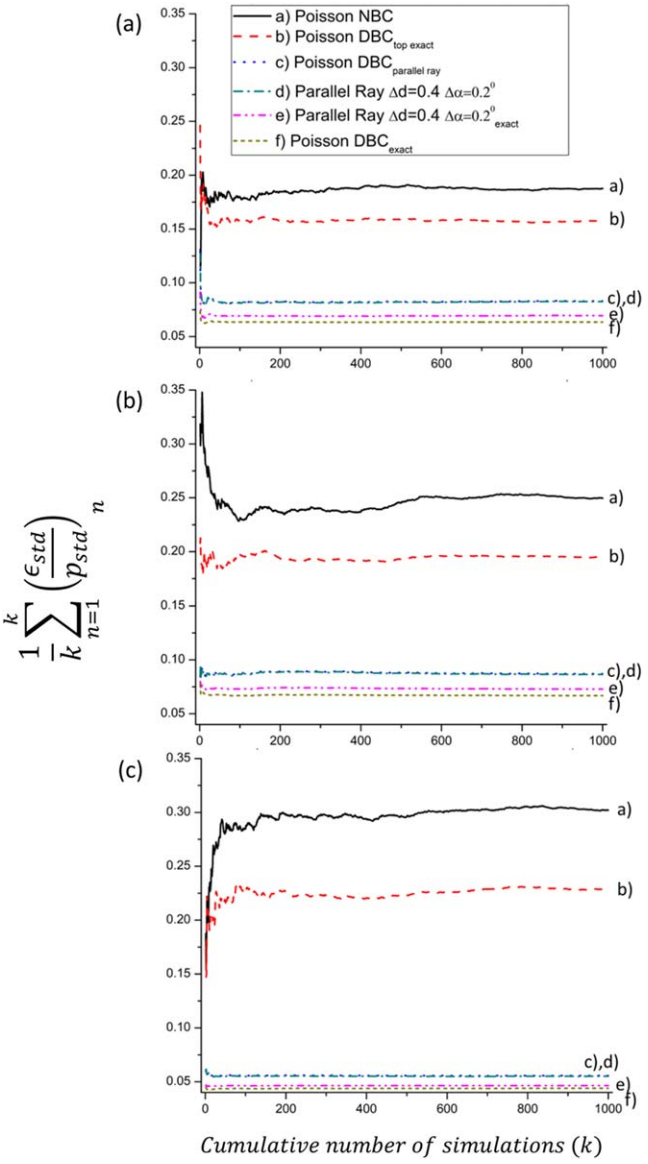

Figure 13. Cumulative average error of pressure reconstructed using different methods from 1000 realizations of pressure gradient fields with (a) 40% random noise superimposed to the central stripe and no noise added elsewhere in the domain; (b) 40% random noise superimposed to the central stripe and 5.0% noise added to the rest of the domain. (c) Gaussian noise superimposed to the entire domain.

pressure reconstruction is to use the so-called mixed boundary conditions [21, 27, 36, etc], where Bernoulli equation is usually used to provide Dirichlet boundary condition in the free stream region on one side of the domain while Neumann boundary condition is used on other boundary sides. To verify the effectiveness of this practice, we use the DNS pressure on top of the domain as Dirichlet boundary condition and applying Neumann boundary condition on other sides of the domain, i.e. Poisson $\mathrm{DBC}_{\mathrm{top_exact}}$ as shown in figure 13. As can be seen in figure 13, this practice (Poisson $\mathrm{DBC}_{\mathrm{top_exact}}$) only outperforms the least accurate method of Poisson NBC, for which Neumann boundary conditions are applied to all boundary points (except one point at the lower-left corner serves as an anchor to provide reference pressure). A summary of the statistics about the accuracy performance for different pressure reconstruction methods are listed in tables 3–5.

To achieve an intuitive understanding of the performance of the two primary pressure reconstruction methods (i.e. parallel ray omnidirectional integration with $\Delta d^* = 0.4, \Delta\alpha = 0.2^\circ$ and Poisson equation method with the Dirichlet boundary condition furnished by the Parallel Ray with $\Delta d^* = 0.4, \Delta\alpha = 0.2^\circ$), figure 14 presents the minimum and maximum ε_{std} error distributions selected from the 1000 reconstructed pressure realizations as representative results for pressure reconstructed from test Case B (40% random noise superimposed to the central stripe and no noise to other places) and Case C (40% random noise superimposed to the central stripe and 5.0% noise added to the rest of the domain), respectively. As shown in figure 14, for both test cases, when ε_{std} is minimum, pressure error values on both top and bottom outsides of the central error embedded region are roughly balanced. However, for the situation with maximum ε_{std}, large pressure error with opposite signs exists across the central region.

To quantify the behaviour about the pressure error propagation from the error-embedded central region to other places within the domain, we define several new quantities, including the ensemble mean, standard deviation and root mean square (rms) distributions based on errors in the reconstructed pressure, as follows:

$$(\varepsilon_{ij})_n = (\tilde{p}_{ij} - p_{ij})_n \tag{32}$$

$$\overline{(\varepsilon_{ij})_n} = \frac{1}{N}\sum_{n=1}^{N}(\varepsilon_{ij})_n \tag{33}$$

$$\varepsilon_{ij_{std}} = \sqrt{\frac{1}{N-1}\sum_{n=1}^{N}\left((\varepsilon_{ij})_n - \overline{(\varepsilon_{ij})_n}\right)^2} \tag{34}$$

$$\varepsilon_{ij_{rms}} = \sqrt{\frac{1}{N-1}\sum_{n=1}^{N}\left|(\varepsilon_{ij})_n\right|^2} \tag{35}$$

$$\overline{\varepsilon_j} = \frac{1}{I_{max}}\sum_{i=1}^{I_{max}}\overline{(\varepsilon_{ij})_n} \tag{36}$$

$$\varepsilon_{j_{std}} = \frac{1}{I_{max}}\sum_{i=1}^{I_{max}}\varepsilon_{ij_{std}} \tag{37}$$

$$\varepsilon_{j_{rms}} = \frac{1}{I_{max}}\sum_{i=1}^{I_{max}}\varepsilon_{ij_{rms}} \tag{38}$$

where n is a dummy variable representing any arbitrary instance of reconstructed pressure realization and N being the total number of realizations. For all the testing cases discussed below, $N = 1000$.

Table 3. Error statistics for pressure reconstructed using different methods from 1000 realizations of pressure gradient field with 40% random noise superimposed to the central stripe and no noise added elsewhere to the domain.

Error statistics	RPR	Poisson DBC RPR	Poisson NBC	RPR Exact BC	Poisson DBC exact	Poisson DBC exact top
$(\varepsilon_{std}\backslash p_{std})_{min}$	0.0559	0.0563	0.0636	0.0528	0.0520	0.0652
$(\varepsilon_{std}\backslash p_{std})_{avg}$	0.0825	0.0830	0.1876	0.0695	0.0635	0.1575
$(\varepsilon_{std}\backslash p_{std})_{max}$	0.1771	0.1777	0.5518	0.1275	0.0985	0.5040
$(\varepsilon_{std}\backslash p_{std})_{std}$	0.0175	0.0175	0.0890	0.0093	0.0054	0.0614

Table 4. Error statistics for pressure reconstructed using different methods from 1000 realizations of pressure gradient field with 40% random noise superimposed to the central stripe and 5.0% noise added to the rest of the domain.

Error statistics	RPR	Poisson DBC RPR	Poisson NBC	RPR Exact BC	Poisson DBC exact	Poisson DBC exact top
$(\varepsilon_{std}\backslash p_{std})_{min}$	0.0610	0.0615	0.0769	0.0578	0.0556	0.0792
$(\varepsilon_{std}\backslash p_{std})_{avg}$	0.0865	0.0870	0.2495	0.0728	0.0668	0.1949
$(\varepsilon_{std}\backslash p_{std})_{max}$	0.1844	0.1870	0.7524	0.1263	0.0935	0.4715
$(\varepsilon_{std}\backslash p_{std})_{std}$	0.0167	0.0168	0.1121	0.0089	0.0053	0.0744

Table 5. Error statistics for pressure reconstructed using different methods from 1000 realizations of pressure gradient field with Gaussian noise superimposed to the entire domain.

Error statistics	RPR	Poisson DBC RPR	Poisson NBC	RPR Exact BC	Poisson DBC exact	Poisson DBC exact top
$(\varepsilon_{std}\backslash p_{std})_{min}$	0.0441	0.0444	0.0759	0.0406	0.0382	0.0677
$(\varepsilon_{std}\backslash p_{std})_{avg}$	0.0551	0.0557	0.3020	0.0464	0.0439	0.2282
$(\varepsilon_{std}\backslash p_{std})_{max}$	0.0813	0.0806	0.8632	0.0570	0.0553	0.7580
$(\varepsilon_{std}\backslash p_{std})_{std}$	0.0056	0.0057	0.1380	0.0028	0.0022	0.1062

Note: RPR, rotation parallel ray ($\Delta d^* = 0.4, \Delta\alpha = 0.2°$); Poisson DBC RPR, Poisson equation with Dirichlet boundary condition based on rotation parallel ray ($\Delta d^* = 0.4, \Delta\alpha = 0.2°$) boundary pressure data; Poisson NBC, Poisson equation with Neumann boundary condition (with the same reference pressure point as other methods); RPR exact BC, rotation parallel ray ($\Delta d^* = 0.4, \Delta\alpha = 0.2°$) with DNS pressure as boundary pressure values; Poisson DBC exact, Poisson equation with DNS pressure as Dirichlet boundary condition; Poisson DBC exact top, Poisson equation with DNS pressure as Dirichlet boundary condition on the topside of the domain and Neumann boundary condition applied to other sides of the domain.

The ensemble mean $\overline{(\varepsilon_{ij})_n}$ and the ensemble standard deviation $\varepsilon_{ij_{std}}$ distributions of reconstructed pressure using the rotation parallel ray omnidirectional integration (with $\Delta d^* = 0.4, \Delta\alpha = 0.2°$) and the Poisson equation method (with converged boundary pressure values generated by the former method as the Dirichlet boundary condition) are compared in figure 15, in the context of their applications to test cases A (40% random error on entire domain), B (40% random noise superimposed to the central stripe and no noise added elsewhere in the domain), C (40% random noise superimposed to the central stripe and 5.0% noise added to the rest of the domain) and D (Gaussian error on entire domain). As can be seen from figure 15, there is virtually no difference between the two pressure reconstruction methods for the four cases investigated, indicating that as long as the converged boundary pressure values are available, the Poisson DBC will generate reconstructed pressure distribution with the same accuracy level as its boundary value feeder, i.e. the parallel ray integration methods. The overall low magnitude ($< 0.01 p_{std}$, i.e. $< 0.002|p|_{max}$) of $\overline{(\varepsilon_{ij})_n}$ shown in figure 15 is due to averaging of the spatial pressure distribution $(\varepsilon_{ij})_n = (\tilde{p}_{ij} - p_{ij})_n$ over the 1000 realizations, which minimizes the influence of the pressure gradient error terms in equations (26) and (27). However, it seems that the truncation errors have been persistently retained through the averaging process, forming sporadic high error concentrations ($\sim 0.05 p_{std}$, i.e. $0.012|p|_{max}$ in magnitude) which are coincident with the areas of high pressure gradient (comparing figures 15 and 6(b)) in the domain.

As shown in figures 15(a) and (b), for cases B and C, although the spatial distribution of the ensemble standard deviation $\varepsilon_{ij_{std}}$ successfully reflects the main feature of embedded pressure gradient error distribution pattern for which high error region appears at the central stripe of the domain, the asymmetric distribution of $\varepsilon_{ij_{std}}$ with respect to the central high error stripe within the domain clearly indicates that there exists an error propagation bias pattern associated with the pressure reconstruction methods investigated. Considering the Poisson $\text{DBC}_{\text{parallel ray}}$ method adopts the converged boundary pressure value generated by the parallel ray method, this error propagation bias pattern is presumably due to the error propagation behaviour through the boundary pressure points during the implementation of the parallel ray omnidirectional integration. Moreover, because the reference pressure is anchored at the lower left corner of the domain, the error propagation in terms of standard deviation $\varepsilon_{ij_{std}}$ has the smallest magnitude in the region surrounding the reference point, and gradually increases its value when the point of interest is getting further away from the reference point, thus

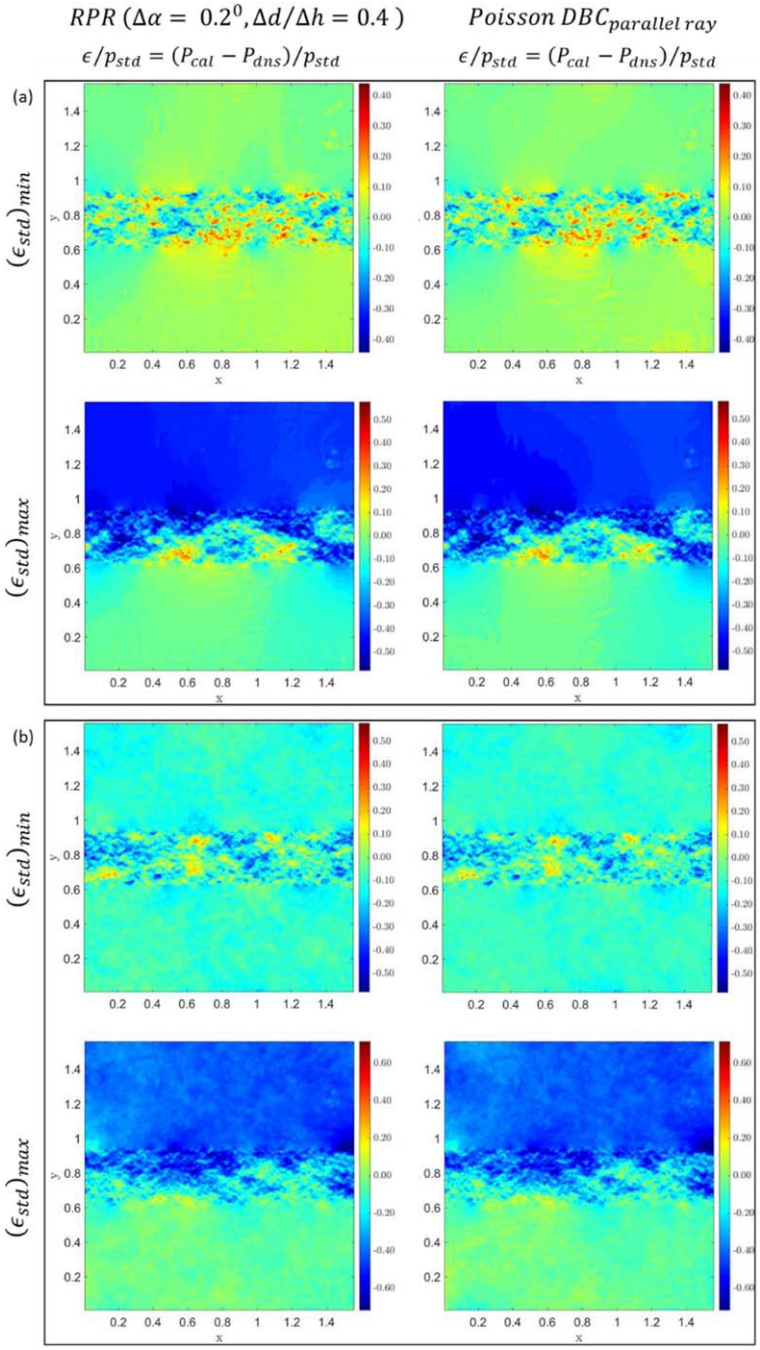

Figure 14. Representative error distributions with maximum and minimum ε_{std} selected from the 1000 pressure realizations reconstructed using parallel ray omnidirectional integration with $\Delta d^* = 0.4$, $\Delta\alpha = 0.2^\circ$ (the first column of plots) and Poisson equation method with Dirichlet boundary condition generated by the parallel ray omni-integration with $\Delta d^* = 0.4, \Delta\alpha = 0.2^\circ$ (the second column of plots) for (a) 40% random noise superimposed to the central stripe and no noise added elsewhere in the domain; (b) 40% random noise superimposed to the central stripe and 5.0% noise added to the rest of the domain.

forming a basin type of error propagation pattern at the area below the horizontal error-embedded stripe (figures 15(a) and (b)). Above the stripe, $\varepsilon_{ij_{std}}$ reaches a higher error plateau ($\sim 0.10 p_{std}$, i.e. $0.02|p|_{max}$), with another basin type of error propagation pattern formed at regions away from the central stripe. Please note that similar basin type distribution patterns for measured $C_{p_{rms}}$ obtained by using virtual boundary omni-directional integration method are also found in the experiment by [12], figures 5(g) and (h) there, as well as figure 18 in this paper about a turbulent shear layer flow past a cavity. Thus to some extent, the basin type distribution patterns for $\varepsilon_{ij_{std}}$ as seen in cases B and C can be viewed as a replica of the actual experiment.

For both Case A (random error entire domain) and Case D (Gaussian error entire domain), there is also a basin type error propagation pattern occurring within the domain, with the reference point serving as the lowest error point within the basin, and the rest of the entire domain serving as a quarter basin

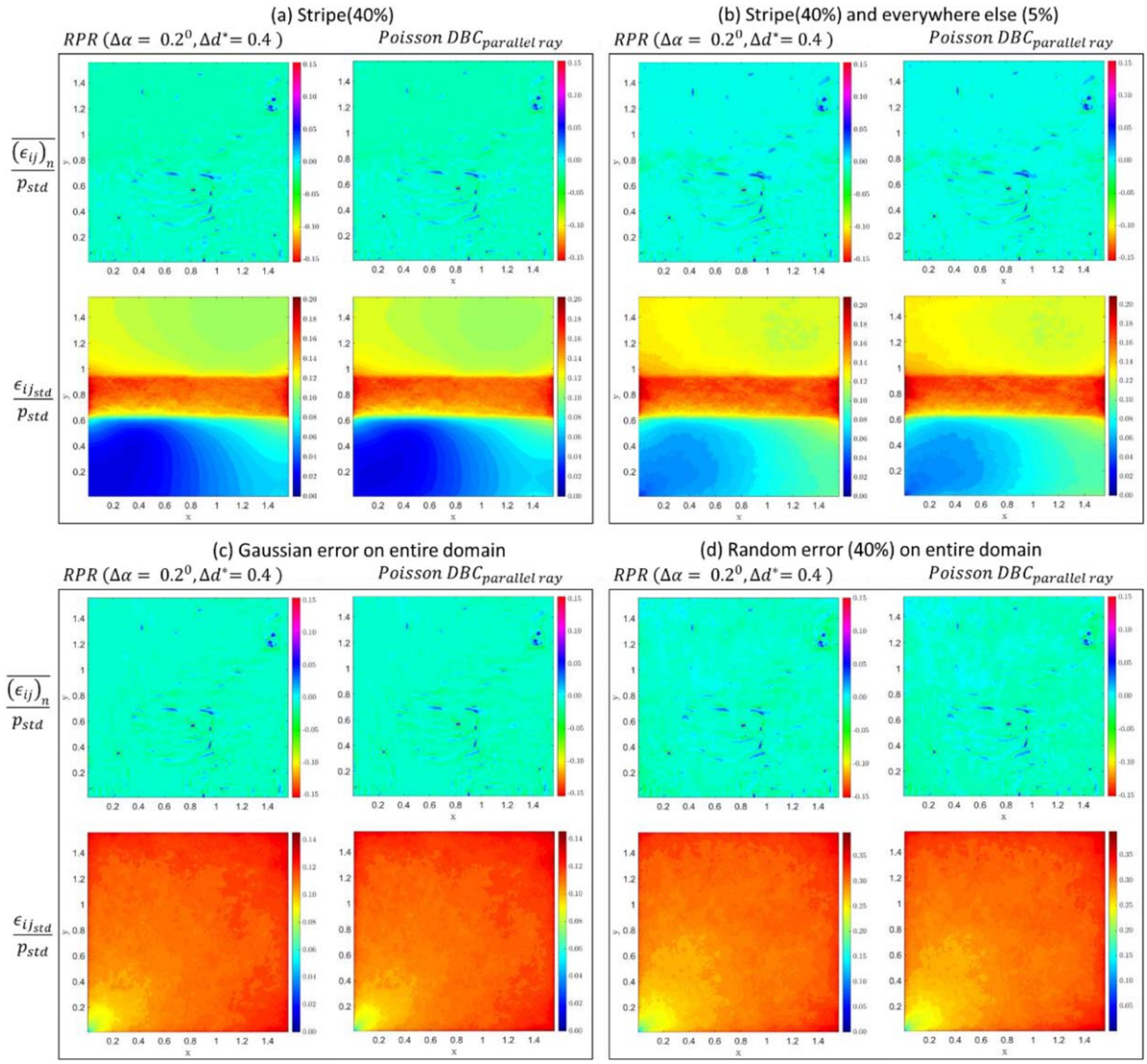

Figure 15. Comparison of mean $\overline{(\varepsilon_{ij})}_n$ and standard deviation $\varepsilon_{ij_{std}}$ error distributions of reconstructed pressure using rotation parallel ray omnidirectional integration with $\Delta d^* = 0.4, \Delta\alpha = 0.2^\circ$ (the first column of plots within each frame) and Poisson equation method with Dirichlet boundary condition generated by the parallel ray omni-integration with $\Delta d^* = 0.4, \Delta\alpha = 0.2^\circ$ (the second column of plots with each frame) for (a) Case B, 40% random noise superimposed to the central stripe and no noise added elsewhere in the domain; (b) Case C, 40% random noise superimposed to the central stripe and 5.0% noise added to the rest of the domain; (c) Case D, Gaussian error on entire domain; and (d) Case A, 40% random error on entire domain.

with gradually elevated standard deviation error $\varepsilon_{ij_{std}}$ at locations away from the basin center, as shown in figures 15(c) and (d), respectively. Because there is no central stripe within the domain, the basin now has a bigger radius compared to that shown in figures 15(a) and (b).

To verify the role that the boundary pressure value plays in determining the error propagation pattern in terms of the ensemble standard deviation $\varepsilon_{ij_{std}}$ distribution, we use DNS boundary pressure value as the converged boundary pressure value for rotation parallel ray omnidirectional integration ($\Delta d^* = 0.4$, $\Delta\alpha = 0.2^\circ$) for test cases A, B, C and D. As a comparison, we also use the DNS boundary pressure value as the Dirichlet boundary condition for the Poisson equation pressure reconstruction implementation for these test cases. Because exact pressure values are used on all boundary points, the $\varepsilon_{ij_{std}}$ distribution becomes more symmetric as shown in figure 16. This is a sharp contrast in comparison with figure 15. The asymmetric pattern of $\varepsilon_{ij_{std}}$ distribution with respect to the central stripe as shown figures 15(a) and (b) now completely disappears. The basin type pattern also disappears in the test cases shown in figure 16.

To facilitate comprehension of the influence of boundary pressure condition and the superimposed pressure gradient error distribution on the reconstructed pressure error propagation using different methods, figure 17 compares the horizontally averaged ensemble standard deviation $\varepsilon_{j_{std}}$, root mean square $\varepsilon_{j_{rms}}$, and mean $\overline{\varepsilon_j}$ error distributions using two methods, i.e. the rotation parallel ray omnidirectional integration ($\Delta d^* = 0.4, \Delta\alpha = 0.2^\circ$) and the Poisson equation Dirichlet boundary condition, with boundary pressure values either (a) generated by rotation parallel ray omnidirectional integration ($\Delta d^* = 0.4, \Delta\alpha = 0.2^\circ$), or (b) set by the exact DNS boundary

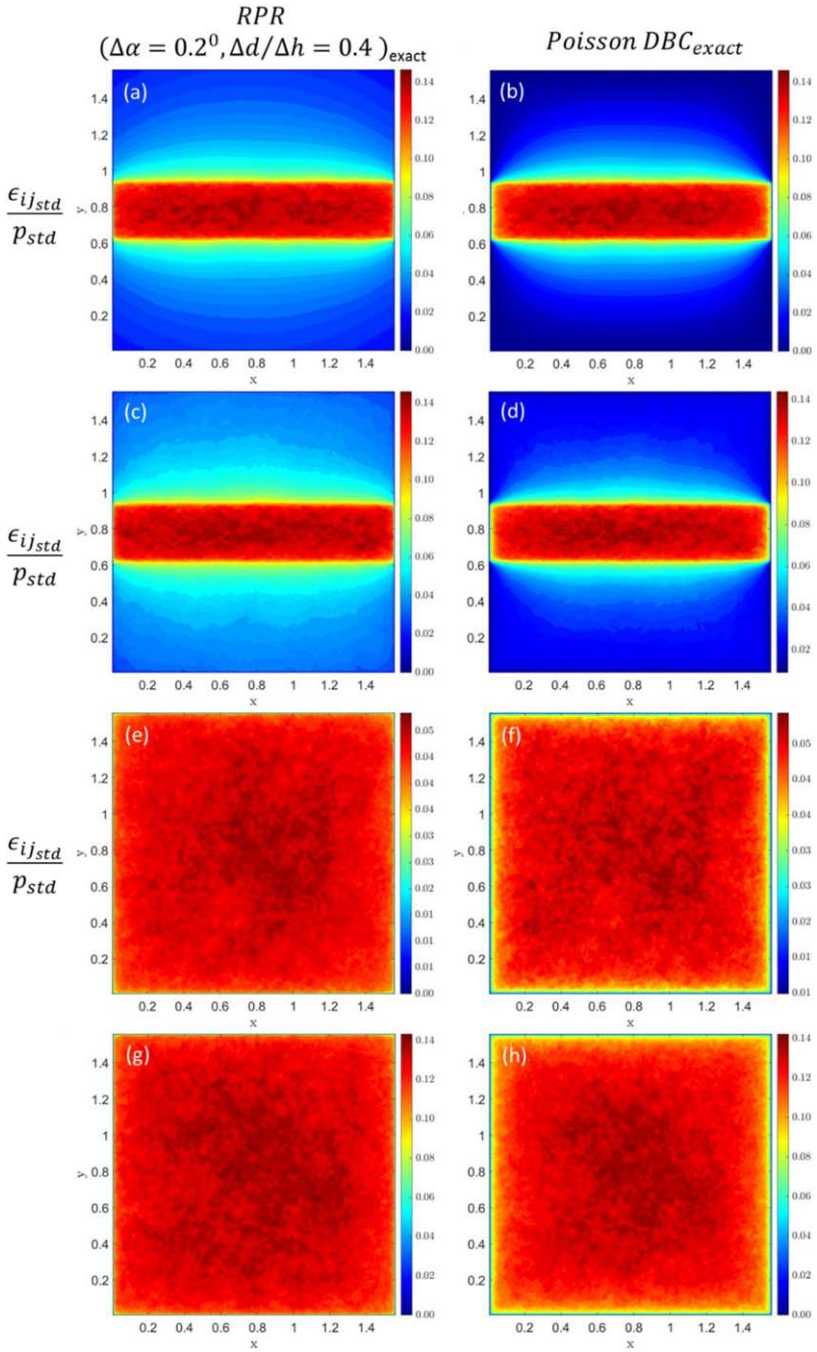

Figure 16. Distribution of ensemble standard deviation of reconstructed pressure error $\varepsilon_{ij_{std}}$ based on DNS boundary pressure value used as, the first column of plots, converged boundary pressure value for rotation parallel ray omnidirectional integration ($\Delta d^* = 0.4, \Delta\alpha = 0.2^\circ$) and, the second column of plots, Dirichlet boundary condition for the Poisson equation pressure reconstruction method. (a) and (b), test Case B, 40% random noise superimposed to the central stripe and no noise added elsewhere in the domain; (c) and (d) test Case C, 40% random noise superimposed to the central stripe and 5.0% noise added to the rest of the domain; (e) and (f) test Case D, Gaussian error on entire domain; and (g) and (h) test Case A, 40% random error on entire domain.

pressure, respectively, for testing cases A (40% all), B (stripe, i.e. 40% error at central stripe), C (mixed, i.e. 40% error at central stripe + 5% elsewhere) and D (Gaussian) embedded error schemes. As can be seen from figure 17, the plots for $\varepsilon_{j_{std}}$ and $\varepsilon_{j_{rms}}$ are very similar. The reason is that, as shown in figure 15 and discussed before, $\overline{(\varepsilon_{ij})}_n$ is small ($< 0.01 p_{std}$) and therefore negligible. Therefore the curves for $\varepsilon_{j_{std}}$ and $\varepsilon_{j_{rms}}$ are almost the same.

As shown in figure 17(a), the superimposed pressure gradient error at the central stripe of the domain results in a hump for the vertical distribution of $\varepsilon_{j_{std}}$ along the y-direction (figure 17 curves a, e, b and f). In front of the hump, the $\varepsilon_{j_{std}}$ curve appears as a valley while behind the hump, there is a plateau. The step difference in $\varepsilon_{j_{std}}$ ($\sim 0.075 p_{std}$, i.e. $\sim 0.018|p|_{max}$) between the plateau and the valley for case B (stripe, i.e. 40% error at central stripe) is reduced to $\sim 0.05 p_{std}$ (i.e. $\sim 0.012|p|_{max}$)

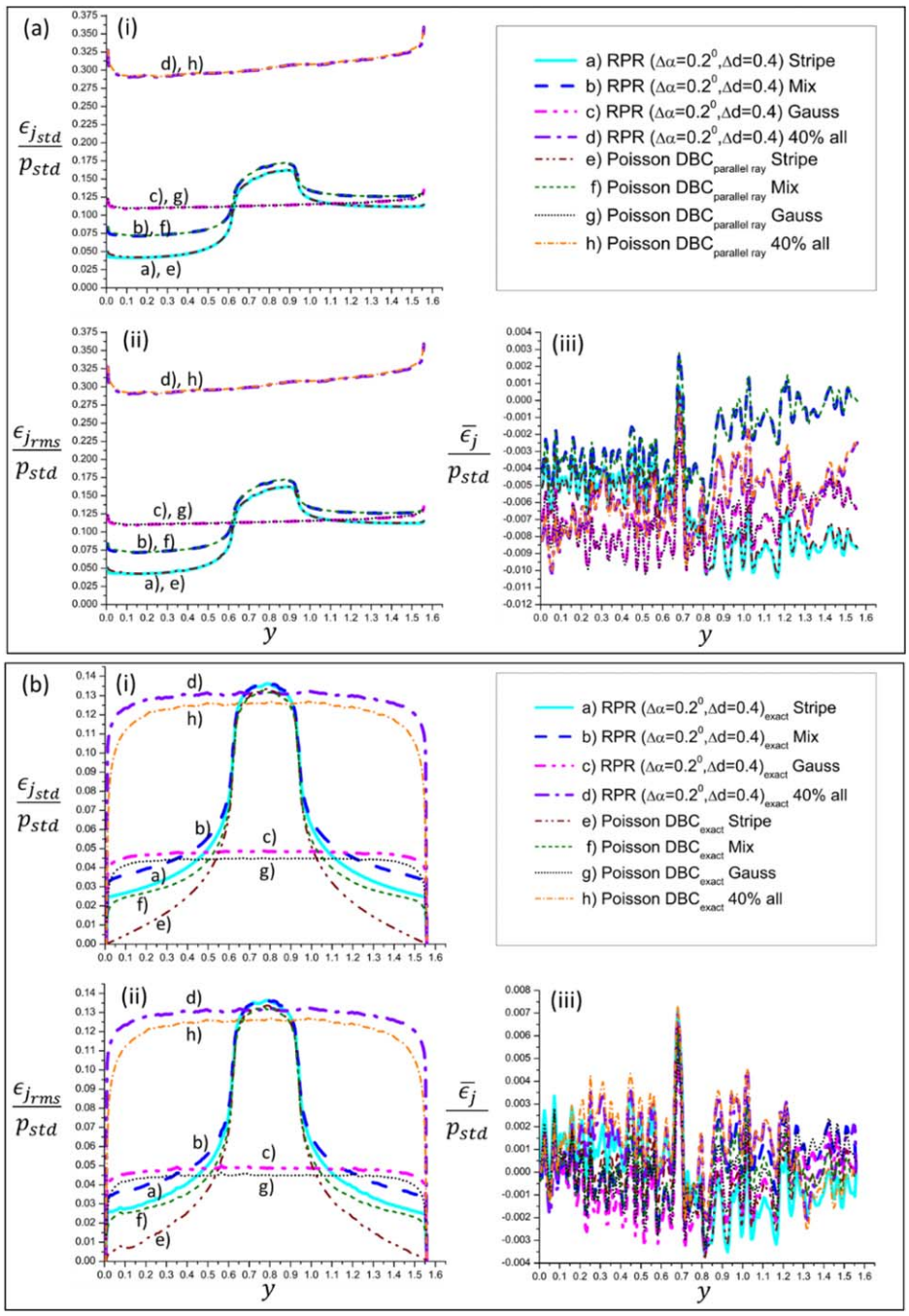

Figure 17. Comparison of horizontally averaged standard deviation $\varepsilon_{j_{std}}$, root mean square $\varepsilon_{j_{rms}}$, and mean $\overline{\varepsilon_j}$ error distributions of reconstructed pressure using two methods, i.e. rotation parallel ray omnidirectional integration ($\Delta d^* = 0.4, \Delta\alpha = 0.2^\circ$) and Poisson equation Dirichlet boundary condition, with boundary pressure values generated by (a) rotation parallel ray omnidirectional integration ($\Delta d^* = 0.4, \Delta\alpha = 0.2^\circ$) and (b) the exact DNS pressure, respectively, for testing cases A (40% all), B (stripe, i.e. 40% error at central stripe), C (mixed, i.e. 40% error at central stripe + 5% elsewhere) and D (Gaussian) embedded error schemes.

for Case C (mixed, i.e. 40% error at central stripe + 5% error elsewhere), indicating the benefits of pressure gradient error cancelation due to the existence of the 5% error region in Case C. If the pressure gradient is homogeneously superimposed with 40% of $\left(|\nabla p|_{DNS}\right)_{max}$ random noise, i.e. test Case A, the $\varepsilon_{j_{std}}$ curve is slanted with an average magnitude difference of $\sim 0.05 p_{std}$, (i.e. $\sim 0.012|p|_{max}$) within the domain range. Similar behaviour is observed for Case D, i.e. the Gaussian pressure gradient error distribution, where a much smaller average magnitude difference of $\sim 0.0125 p_{std}$ (i.e. $\sim 0.003|p|_{max}$) across the domain for the $\varepsilon_{j_{std}}$ curve is observed due to relatively smaller magnitude of pressure gradient error introduced by the Gaussian method (with zero mean and standard deviation of 8.5% of $\left(|\nabla p|_{DNS}\right)_{max}$). The horizontally averaged ensemble mean error $\overline{\varepsilon_j}$ again confirms that across the domain, $\overline{\varepsilon_j} < 0.01 p_{std}$, i.e. $< 0.002|p|_{max}$ for all cases tested, consistent with the discussion before regarding $\overline{(\varepsilon_{ij})_n}$ which is shown in figure 15.

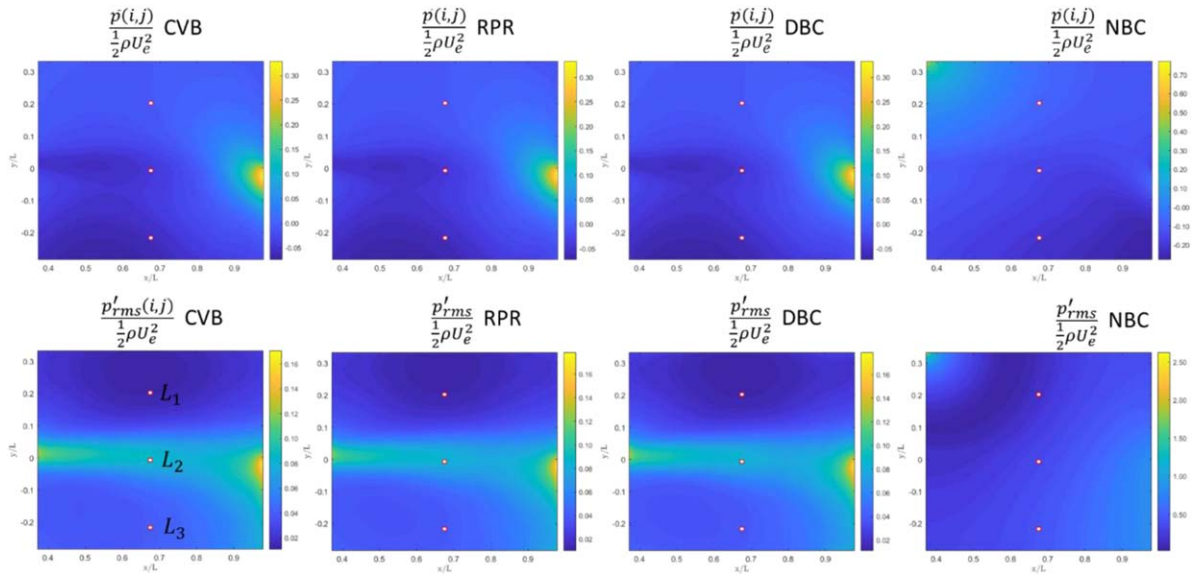

Figure 18. Mean and rms pressure distributions obtained using the circular virtual boundary omnidirectional integration (abbreviated as CVB), the rotational parallel ray omnidirectional integration with $\Delta d^* = 0.4, \Delta\alpha = 0.2°$(RPR), the Poisson equation method with parallel ray generated Dirichlet boundary condition (DBC) and the Poisson equation method with Neumann boundary condition (NBC) pressure reconstruction methods. A total of 9994 sequentially obtained instantaneous realizations of pressure gradient field are involved in the pressure reconstruction for a turbulent shear layer flow over a 2D open cavity at Reynolds number of 4×10^4 based on the cavity length of 38.1 mm and the free stream speed of $U_\infty = 1.20$ m s^{-1}.

As shown in figure 17(b), if DNS pressure is used as the boundary pressure value for the pressure reconstruction, both $\varepsilon_{j_{std}}$ and $\varepsilon_{j_{rms}}$ curves become more symmetric. Please note this is only an ideal situation which is unavailable in real practice.

4.6. Performance of different approaches with experimental data

To verify the performance of the pressure reconstruction methods in processing experimental data, the methods tested in section 4.4 are also applied to pressure reconstruction from the measured pressure gradient field database for a turbulent shear layer flow over an open cavity [3, 12]. The results are compared in terms of mean and rms pressure distributions (figure 18) as well as probability density function profiles of pressure fluctuations at selected locations in the shear layer (figure 19). The experiment regarding the turbulent cavity shear layer flow has been described in detail in Liu and Katz [3, 12]. A turbulent boundary layer with a shape factor of 1.70 separates from the leading edge of a 2-D open cavity, forming a turbulent shear layer over the cavity. Time-resolved planar PIV data, sampled at 4500 frames per second, have been obtained at a Reynolds number of 4.0×10^4 based on the cavity length of 38.1 mm and the free stream speed of $U_\infty = 1.20$ m s^{-1}. The pressure gradient field has been obtained based on the Lagrangian acceleration measurement, as discussed in section 2.1. A sample of 9994 sequentially obtained instantaneous realizations of pressure gradient field with a field of view of 25 × 25 mm located immediately upstream of the cavity trailing edge are utilized in the current study to compare the pressure reconstruction performance.

From figure 18, it can be seen that, similar to the performance comparison results based on the embedded error in the isotropic turbulence discussed in section 4.4, for the experimental data, except the Poisson equation NBC approach, the performance for the other three pressure reconstruction methods evaluated, i.e. the the circular virtual boundary omnidirectional integration, the rotational parallel ray omnidirectional integration $(\Delta d^* = 0.4, \Delta\alpha = 0.2°)$, and the Poisson equation method with parallel ray generated Dirichlet boundary condition can all capture the essential features of the mean and rms pressure distributions if compared with the corresponding results in Liu and Katz [12]. In contrast, the Poisson equation with Neumann boundary condition fails to capture the pressure field correctly.

To further verify the above results, figure 19 shows the comparison of the probability density function profiles for the fluctuation pressure obtained by these four pressure reconstruction methods at representative sample locations L_1 (at the free stream region), L_2 (in the shear layer) and L_3 (in the cavity recirculation region) as indicated in figure 18. It can be seen that, except the result obtained by the Poisson equation with Neumann boundary condition, the fluctuation pressure range predicted by the other three methods agree with each other. The mismatch at the tails of the profiles shown in figures 19(d)–(f) is presumably due to lack of convergence due to the rare flow events corresponding to those fluctuation range. In contrast, the Poisson equation with Neumannboundarycondition once again brings a significantly over-predicted pressure fluctuation range, which is unrealistic.

5. Conclusion

Characterization of the accuracy performance and the error propagation properties of the PIV pressure reconstruction

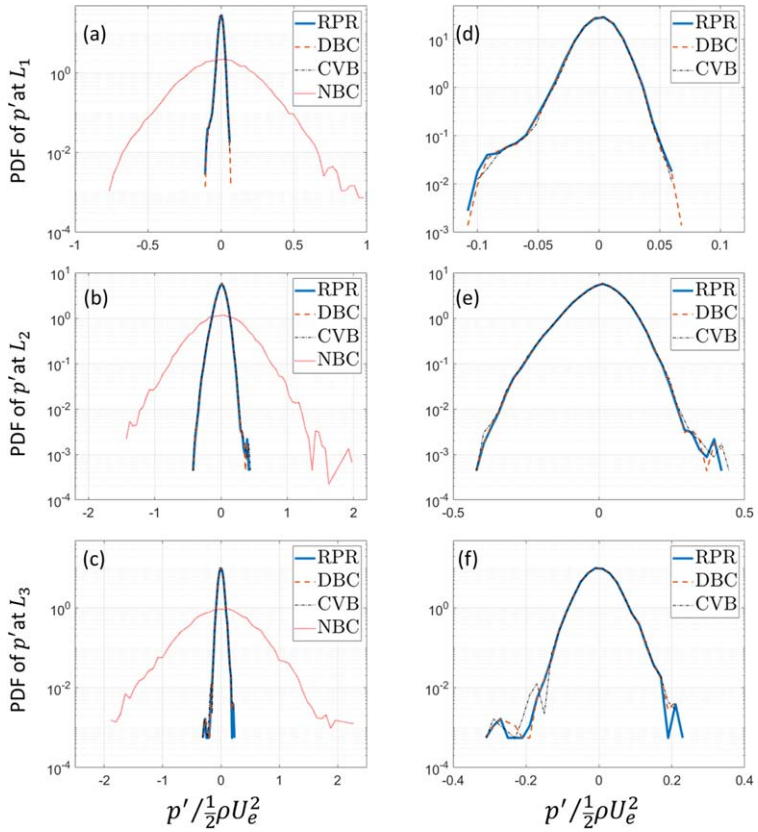

Figure 19. Comparison of the probability density function profiles for the fluctuation pressure at sample locations L_1, L_2 and L_3 as indicated in figure 18 for a turbulent shear layer flow over a 2D open cavity at Reynolds number of 4.0×10^4. The pressure data are obtained by using the circular virtual boundary omnidirectional integration (abbreviated as CVB), the rotational parallel ray omnidirectional integration with $\Delta d^* = 0.4, \Delta\alpha = 0.2^\circ$ (RPR), the Poisson equation method with parallel ray generated Dirichlet boundary condition (DBC) and the Poisson equation method with Neumann boundary condition (NBC) pressure reconstruction methods. The right column PDF profiles are zoomed-in plots for the corresponding left column PDF plots.

methods is of critical importance in understanding their capabilities and limitations. This paper presents for the first time a comprehensive theoretical analysis and numerical verification of the error propagation behaviour from the PIV-based pressure gradient to the reconstructed pressure by using the omnidirectional integration methods, and demonstrates the critical importance of accurate determination of the boundary pressure values in ensuring the accuracy for the final reconstructed pressure distribution in an error-embedded turbulent flow field.

The omnidirectional integration provides an effective boundary pressure error reduction mechanism through iteration. The error in the boundary pressure value $(\varepsilon_n^{(q+1)})$ effectively consists of two parts. One part $(\varepsilon_{\mathrm{nB}}^q)$ decreases in magnitude exponentially at characteristic error decay rate $\lambda_{n,max}(|\lambda_{n,max}| < 1)$ and eventually vanishes through an iteration process, the other $(\varepsilon_{nA} + \varepsilon_{ref})$ remains a constant of small magnitude for a given pressure gradient field during the iteration. As a result, the boundary pressure value eventually converges to a small error characterized by $(\varepsilon_{nA} + \varepsilon_{ref})$. Theoretical analysis based on non-homogeneous linear recurrence theory supports the above observation. As long as the pressure gradient error is random and homogeneously distributed, the spatial integration and the averaging process will lead to a small final value in ε_{nA}.

The pressure at the inner domain requires only a one-step calculation after the pressure at boundary points reach a converged solution. At inner nodal points, the pressure error depends only on (1) the summation of the truncation error of integration scheme and (2) the integration of the pressure gradient error. It does not change in magnitude with boundary pressure value iteration.

The error propagation analysis shows that increase in the density of the integration path not only helps expedite the decrease of the error, but also increase the accuracy of the final reconstructed pressure. For a domain of 254×254 nodal points, $\Delta\alpha \approx 0.1 - 0.2^\circ$ and $0.35 < \Delta d^* < 0.71$ are the recommended ranges for the parallel ray omnidirectional integration parameter selection.

The accuracy performance of the omnidirectional integration methods is further investigated using error-embedded DNS isotropic turbulence in the context of comparison with Poisson equation based pressure reconstruction methods. Temporally statistical independent noise at various noise levels and with different noise spatial distribution schemes are

superimposed to the pressure gradient fields of the DNS isotropic turbulence for the investigation. Results indicate that overall the omnidirectional methods give better accuracy of the reconstructed pressure in terms of both average and standard deviation errors than the Poisson equation methods with either entire (except the reference point as Dirichlet) or partial (with top domain side using Dirichlet) Neumann boundary conditions, and the disparity between these two types of methods becomes more evident when the imposed noise level increases. Representative results in terms of the average error of the reconstructed pressure based on 1000 statistically independent pressure gradient field realizations with a noise amplitude of 40% of $(|\nabla p|_{DNS})_{max}$ is 0.854 ± 0.406 for the pressure Poisson equation with Neumann boundary condition, 0.154 ± 0.015 for the circular virtual boundary omnidirectional integration method and 0.149 ± 0.015 for the rotating parallel ray omnidirectional integration method, indicating the low sensitivity of the omnidirectional integration to random noise in comparison with the conventional Poisson method. If the converged boundary pressure values obtained by the rotating parallel ray are used as the Dirichlet boundary conditions to feed into the pressure Poisson solver, the nondimensionalized average error for the reconstructed pressure by Poisson is reduced to 0.151 ± 0.015, i.e. the same level of accuracy as those of the omnidirectional integration approaches, demonstrating the benefit brought by the omnidirectional integration method in providing correct boundary conditions for Poisson solvers. Of the different variations of the omnidirectional methods, the parallel ray method shows the best performance capability for all noise distribution schemes tested (including random or Gaussian noise on entire domain, and elevated noise at central stripe of domain), and therefore is the method of choice.

Comparison of pressure error spectrum based on 40% noise in entire pressure gradient domain indicates that except Poission NBC, most error contributions occur at the high wave number space, implying error propagation remains locally. This understanding is consistent with the pressure error distribution analysis based on the DNS data superimposed with artificial error.

The performance of these pressure reconstruction methods are also compared for a turbulent shear layer flow over an open cavity. The comparison results in terms of the mean and rms pressure distributions as well as the fluctuating pressure PDF distributions at selected locations in the flow field are consistent with the conclusion based on the DNS simulation data, i.e. the omnidirectional integration methods outperforms the Poisson equation approach with Neumann boundary conditions.

The step difference between the plateau and valley beside the central error elevation stripe, and the basin type of error propagation pattern as revealed in standard deviation error $\varepsilon_{ij_{std}}$ or rms error $\varepsilon_{ij_{rms}}$ distributions for the error-embedded simulation realizations represent the major limitations for omnidirectional integration methods in determining pressure fluctuation statistics. However, these shortcomings have also been seen in Poisson equation approaches and therefore are not unique to the omnidirectional integration methods. Actually the omnidirectional integration methods as represented by the parallel ray are capable of minimizing these shortcomings in error propagation. Therefore even with these shortcomings, the omnidirectional integration methods especially the parallel ray are still the methods of choice. The influence due to these shortcomings is below 2% of the maximum pressure according to current study based on the DNS data embedded with artificial error. How to further reduce or completely eliminate these shortcomings require further investigation.

Please note that in actual PIV velocity fields, errors associated with velocity data are spatially correlated. Therefore, spatially uncorrelated random error superimposed onto the pressure gradient components may not be a realistic representation of the type of error that is actually seen in the measured pressure gradients. In a follow-up work, a better error model using a filter of defined width applied to the random error fields and rescaled to have the proper magnitude to create a spatial error covariance similar to that found in PIV measurements will be incorporated. Simulation of such pressure gradient error fields with typical characteristics (particularly covariances) inherited from velocity error will verify whether such error characteristics cause issues in the reconstructed pressure field.

Since there are numerous occasions in science and engineering practice that require solution of a scalar potential from a conservative vector field using Poisson equation, e.g. the reconstruction of temperature or wavefront from their corresponding error-embedded gradients, the omnidirectional integration methods, especially the parallel ray omnidirectional integration method, are readily applicable to those generic occasions in scalar reconstruction from their error contaminated gradient data.

Acknowledgments

This work has been sponsored in part by the San Diego State University UGP program 2015, the Office of Naval Research Grant No. N00014-19-1-2020 (K.-H. Kim is the Program Officer), and National Science Foundation Grant No. 1933176 (R Joslin is the Program Director). The authors would like to thank Professor J Katz for his permission of the use of the Hopkins cavity research data in this study. The help from Dr Minping Wan and Professor Charles Meneveau in retrieving the DNS data from JHTDB is gratefully acknowledged. The insightful comments from the reviewers of the paper are also highly appreciated. J R Moreto acknowledges the support of the 2018/19 University Graduate Fellowship from the San Diego State University. Both authors contributed equally to this paper.

Appendix A

Following the definition and the discussion about the error propagation analysis presented in section 3, and plugging the pressure decomposition equation (5) and the error definition

equation (11) into equation (6), we obtain

$$\tilde{p}_n^{(q+1/2)} = \frac{1}{N_n}\sum_{l=1}^{M}\left[R(l,n)\left(p_l + \varepsilon_l^q + \int_{s_l}^{s_n}\nabla p\cdot\boldsymbol{ds} + \int_{s_l}^{s_n}\varepsilon_{\nabla p}\cdot\boldsymbol{ds}\right)\right]. \tag{39}$$

Recognizing that

$$p_l + \int_{s_l}^{s_n}\nabla p\cdot\boldsymbol{ds} = p_n + \varepsilon_{t_{(l,n)}} \tag{40}$$

where the $\varepsilon_{t_{(l,n)}}$ is the truncation error due to the numerical method used for integration along the path connecting point s_l to point s_n. Please note the integral sign throughout the paper is in a sense of numerical integration.

Plugging equation (40) into equation (39), and considering the relationship between N_n and $R(l,n)$ as defined in equation (7), we have

$$\tilde{p}_n^{(q+1/2)} = p_n + \frac{1}{N_n}\sum_{l=1}^{M}\left[R(l,n)\left(\varepsilon_l^q + \varepsilon_{t_{(l,n)}} + \int_{s_l}^{s_n}\varepsilon_{\nabla p}\cdot\boldsymbol{ds}\right)\right]. \tag{41}$$

Using equation (41), we compute the correction term as defined in equation (8):

$$\Delta_{ref}^{q+1/2} = \tilde{p}_{ref} - \left[p_r + \frac{1}{N_r}\sum_{l=1}^{M}R(l,r) \times\left(\varepsilon_l^q + \varepsilon_{t_{(l,r)}} + \int_{s_l}^{s_r}\varepsilon_{\nabla p}\cdot\boldsymbol{ds}\right)\right]. \tag{42}$$

Applying the correction equation (42) to equation (41), using the relationship defined in equation (9), we have

$$\tilde{p}_n^{(q+1)} = p_n + \tilde{p}_{ref} - p_r + \sum_{l=1}^{M}\left[\frac{R(l,n)}{N_n}\left(\varepsilon_l^q + \varepsilon_{t_{(l,n)}} + \int_{s_l}^{s_n}\varepsilon_{\nabla p}\cdot\boldsymbol{ds}\right) - \frac{R(l,r)}{N_r}\left(\varepsilon_l^q + \varepsilon_{t_{(l,r)}} + \int_{s_l}^{s_r}\varepsilon_{\nabla p}\cdot\boldsymbol{ds}\right)\right]. \tag{43}$$

Rearranging equation (43),

$$\left(\tilde{p}_n^{(q+1)} - p_n\right) = (\tilde{p}_{ref} - p_r) + \varepsilon_{nA} + \varepsilon_{nB}^q. \tag{44}$$

From the error definitions equations (10) and (11), we can obtain

$$\varepsilon_n^{q+1} = \varepsilon_{ref} + \varepsilon_{nA} + \varepsilon_{nB}^q \tag{45}$$

where

$$\varepsilon_{nA} = \sum_{l=1}^{M}\left[\frac{R(l,n)}{N_n}\left(\varepsilon_{t_{(l,n)}} + \int_{s_l}^{s_n}\varepsilon_{\nabla p}\cdot\boldsymbol{ds}\right) - \frac{R(l,r)}{N_r}\left(\varepsilon_{t_{(l,r)}} + \int_{s_l}^{s_r}\varepsilon_{\nabla p}\cdot\boldsymbol{ds}\right)\right] \tag{46}$$

and

$$\varepsilon_{\mathrm{nB}}^q = \sum_{l=1}^{M}\left(\frac{R(l,n)}{N_n} - \frac{R(l,r)}{N_r}\right)\varepsilon_l^q. \tag{47}$$

Note that the term ε_{nA} does not depend on the iterations. The first parenthesis on the right-hand side (RHS) of the equation (46) is composed of the numerical truncation error $\varepsilon_{t_{(l,n)}}$ for the pressure integration along the path connecting point s_l to s_n and the integral of the embedded error in the pressure gradient $\varepsilon_{\nabla p}$ along that path. The second parenthesis on the RHS of the equation (46) is composed of the numerical truncation error $\varepsilon_{t_{(l,r)}}$ for the pressure integration along the path connecting point s_l to s_r and the integral of the embedded error in the pressure gradient $\varepsilon_{\nabla p}$ along that path. N_n and N_r are the number of paths involved on the calculation of the pressure update for the node s_n and s_r respectively, and are determined by equation (7).

We can write equation (47) as a weighted summation of the errors (ε_l) involved in the operation, where the weights $w(l,n)$ depend on the scheme of rays connecting the boundary points (i.e. virtual boundary omnidirectional integration or parallel ray integration, etc):

$$\varepsilon_{\mathrm{nB}}^q = \sum_{l=1}^{M}\left(w(l,n)\cdot\varepsilon_l^q\right) \tag{48}$$

where

$$w(l,n) = \frac{R(l,n)}{N_n} - \frac{R(l,r)}{N_r} \tag{49}$$

For a given measurement domain, the weight $w(l,n)$ depends only on the omnidirectional integration method used in the pressure reconstruction. It does not depend on the noise level in the measured pressure gradient field. For the rotating parallel ray method, the weight $w(l,n)$ depends on the ray density, i.e. the parameter of $(\Delta\alpha, \Delta d^*)$. Increasing the ray density decreases the weight magnitude.

Plugging equation (48) back into equation (45):

$$\varepsilon_n^{q+1} = \sum_{l=1}^{M}\left(w(l,n)\cdot\varepsilon_l^q\right) + \varepsilon_{ref} + \varepsilon_{nA}. \tag{50}$$

It can be seen from equation (50) that ε_n^{q+1} depends on ε_n^q (when $l = n$). Since the boundary node s_n connects to other boundary point s_l, the error ε_l^q at point s_l and iteration q also depends on the error ε_n^{q-1} at point s_n at iteration $q-1$ according to equation (50). From this recurrent dependence of the pressure error on its own values at previous iterations, equation (48) can be rewritten as

$$\varepsilon_{\mathrm{nB}}^q = \sum_{l=1}^{M}\left(w(l,n)\cdot\varepsilon_l^q\right) = a_{n,0} + \sum_{p=1}^{q}a_{n,p}\varepsilon_n^p,\ q > 0 \tag{51}$$

where $a_{n,p}$ are coefficients based on the omnidirectional integration algorithm. Assuming $a_{n,p}$ are constant coefficients, and

plugging equations (51) to (45), we have

$$\varepsilon_n^{q+1} - \sum_{p=1}^{q} a_{n,p}\varepsilon_n^p = \varepsilon_{ref} + \varepsilon_{nA} + a_{n,0} \tag{52}$$

Equation (52) is a non-homogenous linear recurrence. According to Mariconda and Tonolo [63], the general solution to equation (52) can be obtained by adding a particular solution to the general solution of the associated homogeneous recurrence. An order q recurrence has an order q characteristic polynomial which has m distinct complex roots λ_m of multiplicity $\mu_1, \ldots, \mu_m$. Therefore, the general solution for the homogeneous linear recurrence associated with equation (52) is

$$\varepsilon_n^q = \sum_{p=1}^{m} \left(P_{n,p}(q) \cdot (\lambda_{n,p})^q \right) \tag{53}$$

where $\lambda_{n,p} (p = 1, \ldots, m)$ are the distinct roots of the characteristic polynomials, and $P_{n,p}(q)$ are polynomials of degree strictly less than the corresponding multiplicity μ_p. Furthermore, for an omnidirectional integration algorithm such as the parallel ray omnidirectional integration with sufficiently dense rays, the error converges as can be seen from figure 8, implying that $|\lambda_{n,p}| < 1 \forall n,p$. Therefore, after sufficient iterations ($q \gg 1$), the term with the largest magnitude $(\lambda_{n,max})$ dominates the solution. Thus, the solution to equation (52) for $q \gg 1$ can be written as

$$\varepsilon_n^q = P_{n,max}(q)\,\lambda_{n,max}^q + f(q) \tag{54}$$

where $P_{n,max}(q)$ is the polynomial of degree less than the multiplicity of the characteristic polynomial root $\lambda_{n,max}$ and $f(q)$ is the particular solution for equation (52). We can evaluate the particular solution, because when $|\lambda_{n,max}| < 1$, the first term on the RHS of equation (54) is negligible for large q. As a result

$$\varepsilon_n^{q\infty} = f(q). \tag{55}$$

Inspecting figure 8, we can see that $\varepsilon_{nB}^q \approx 0$ when q is sufficiently large, and the error ε_n^q converges to ε_{nA}. Note that for both cases shown in figure 8, $\varepsilon_{ref} = 0$. According to equation (45), to incorporate ε_{ref} for the general case, we have

$$\varepsilon_n^{q\infty} = \varepsilon_{ref} + \varepsilon_{nA} = f(q). \tag{56}$$

Plugging equation (56) into equation (54), we have

$$\varepsilon_n^q = P_{n,max}(q)\,\lambda_{n,max}^q + \varepsilon_{ref} + \varepsilon_{nA} \tag{57}$$

i.e.

$$\varepsilon_n^q - (\varepsilon_{ref} + \varepsilon_{nA}) = P_{n,max}(q)\,\lambda_{n,max}^q. \tag{58}$$

Taking the logarithm of equation (58):

$$\log_{10}|\varepsilon_n^q - (\varepsilon_{ref} + \varepsilon_{nA})| = q\log_{10}|\lambda_{n,max}| + \log_{10}|P_{n,max}(q)|. \tag{59}$$

When the solution is converged, $q = q_{end}$:

$$\varepsilon_n^{q_{end}} \approx \varepsilon_{ref} + \varepsilon_{nA} \tag{60}$$

according to equation (56). From equations (59) and (60)

$$\log_{10}|\varepsilon_n^q - \varepsilon_n^{q_{end}}| = q\log_{10}|\lambda_{n,max}| + \log_{10}|P_{n,max}(q)|. \tag{61}$$

Equation (61) is valid for large q when the polynomial root $\lambda_{n,max}$ dominates the solution. This hypothesis is checked by finding $\lambda_{n,max}$ for all boundary points (figure 20(a)) using linear regression based on equation (61) and inspecting the coefficient of determination R^2 for linearity verification at each boundary point as shown in figure 20(b). To facilitate a conservative evaluation, the maximum absolute values of the characteristic error decay rate of the boundary pressure error for all boundary points at different parallel ray configuration and noise conditions (e.g. with and without added noise) are listed in table A1. Two cases were evaluated, one without noise and one with 40% noise embedded in the pressure gradient. For each case the pressure was reconstructed using the rotating parallel ray method with parameter combinations of $\left(\Delta\alpha = 0.04^0, \Delta d^* = 0.4\right)$, $\left(\Delta\alpha = 0.2^0, \Delta d^* = 0.4\right)$, $\left(\Delta\alpha = 3.0^0, \Delta d^* = 0.4\right)$, respectively. The linear region was established starting from iteration $q = 8$ up to $q = 28$ for all three parameter combinations. When $q > 28$, the error differences $(\varepsilon_n^q - \varepsilon_n^{q_{end}})$ are below the floating-point relative accuracy of 2.2204×10^{-16}. As shown in figure 20(b), in the linear region, R^2 is greater than 0.998 for the cases with high or good ray densities, i.e. $\left(\Delta\alpha = 0.04^0, \Delta d^* = 0.4\right)$ or $\left(\Delta\alpha = 0.2^0, \Delta d^* = 0.4\right)$. For the worst case with low ray density, i.e. $\left(\Delta\alpha = 3.0^0, \Delta d^* = 0.4\right)$, R^2 can be as low as 0.825. In the linear region all boundary point solutions are convergent, indicating $|\lambda_{n,max}| < 1$. Moreover, the rate of convergence $(1/\lambda_{n,max})$ increases as the ray density increases, e.g. $max(|\lambda_{n,max}|) = 0.36$ for $\left(\Delta\alpha = 0.04^0, \Delta d^* = 0.4\right)$, and $max(|\lambda_{n,max}|) = 0.57$ for $\left(\Delta\alpha = 3.0^0, \Delta d^* = 0.4\right)$, as indicated in the legend of figure 20(a). The fact that R^2 is very close to unity for high ray density indicates that equation (61) is linear on q, and the second term on the RHS of equation (61), i.e. $\log_{10}|P_{n,max}(q)|$ does not depend on q, implying that $P_{n,max}(q)$ is a constant $(C_{n,max})$. The solution to the non-homogeneous linear recurrence (equation 52) for $q \gg 1$ can now be expressed as

$$\varepsilon_n^q = \lambda_{n,max}^q C_{n,max} + \varepsilon_{nA} + \varepsilon_{ref}. \tag{62}$$

In the linear region, the slope (i.e. $\log_{10}|\lambda_{n,max}|$) of the error convergence curve depends on the number of rays, because $\lambda_{n,max}$ is a function of the ray connection scheme. However, $\lambda_{n,max}$ does not depend on the noise level (as shown in figures 20 and 21), nor the initial condition (as shown in figure 3). On the other hand, the constant $C_{n,max}$ depends on the initial condition (figure 3), the ray connection scheme (figure 21), and the noise level (figures 20 and 21), thus changing the elevation $(\log_{10}|C_{n,max}|)$ of the error convergence curve.

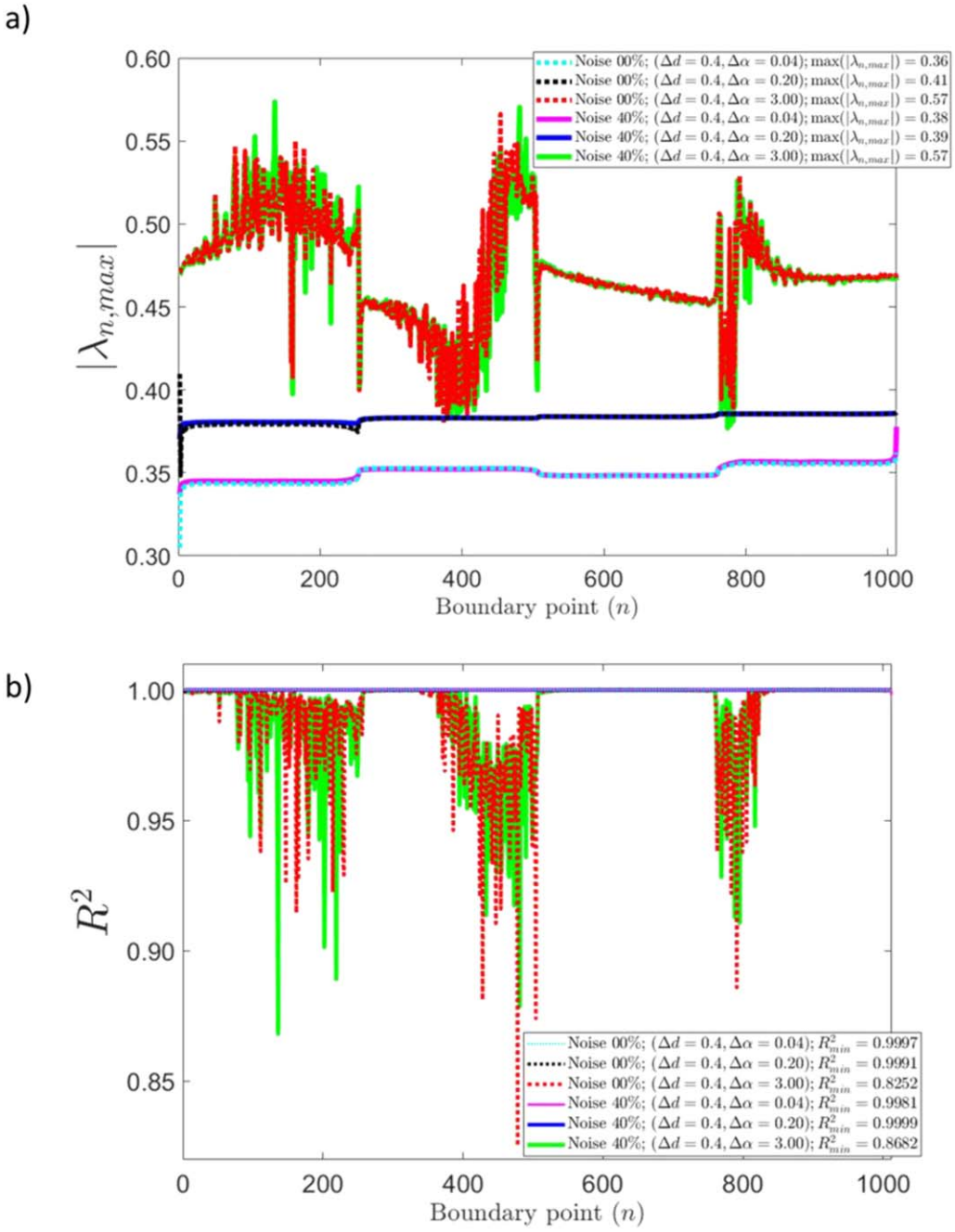

Figure 20. (a) Variation of characteristic error decay rate $|\lambda_{n,max}|$ with each boundary point n for parallel ray omnidirectional integration methods with different parallel ray parameters (Δd^* and $\Delta\alpha$ values). The characteristic error decay rate $|\lambda_{n,max}|$ at every boundary point is determined from linear regression of boundary pressure error $\log_{10}|\varepsilon_n^q - \varepsilon_n^{q_{end}}|$ with respect to iteration number q according to equation (61) based on the pressure reconstructed using the rotating parallel ray omnidirectional method from the DNS isotropic turbulence flow pressure gradient field with and without 40% noise embedded in the entire domain. (b) The coefficient of determination R^2 determined at each boundary point n for the linear regression of boundary pressure error $\log_{10}|\varepsilon_n^q - \varepsilon_n^{q_{end}}|$ with respect to iteration number q according to equation (61)

As an additional validation case, we use the original omnidirectional method [8] to verify the solution shown in equation (62). For the original omnidirectional method, all boundary points connect to each other only once. Therefore,

$$\begin{cases} R(i,j) = 0 \text{ if } i = j \\ R(i,j) = 1 \text{ if } i \neq j \end{cases}. \tag{63}$$

From the definition equations (63) and (47)

$$\varepsilon_{nB}^q = \frac{1}{N_n}\left(\varepsilon_r^q - \varepsilon_n^q\right). \tag{64}$$

Noticing that $\varepsilon_r^q \equiv \varepsilon_{ref}$ and plugging equation (64) into equation (45):

$$\varepsilon_n^{q+1} = \varepsilon_{ref} + \varepsilon_{nA} + \frac{1}{N_n}\left(\varepsilon_{ref} - \varepsilon_n^q\right). \tag{65}$$

Table A1. The maximum value selected from the boundary pressure characteristic error decay rate associated with each boundary point.

Percentage noise added (%)	Parallel ray configuration parameters	The maximum characteristic error decay rate $(\lvert\lambda_{n,max}\rvert)_{max}$	The minimum coefficient of determination $(R^2)_{min}$
0.0	$(\Delta\alpha = 0.04°,\ \Delta d^* = 0.4)$	0.36	0.9997
0.0	$(\Delta\alpha = 0.20°,\ \Delta d^* = 0.4)$	0.41	0.9991
0.0	$(\Delta\alpha = 3.00°,\ \Delta d^* = 0.4)$	0.57	0.8252
40.0	$(\Delta\alpha = 0.04°,\ \Delta d^* = 0.4)$	0.38	0.9981
40.0	$(\Delta\alpha = 0.20°,\ \Delta d^* = 0.4)$	0.39	0.9999
40.0	$(\Delta\alpha = 3.00°,\ \Delta d^* = 0.4)$	0.57	0.8682

If the errors of the initial pressure values at the boundary points are ε_n^0, the solution to the error convergence (equation 65) at the boundary points for the original omnidirectional method can be obtained by following the procedure in Mariconda and Tonolo [63], which gives

$$\varepsilon_n^q = \left(-\frac{1}{N_n}\right)^q \left(\varepsilon_n^0 - \varepsilon_{ref} - \frac{N_n}{N_n+1}\varepsilon_{nA}\right) + \varepsilon_{ref} + \frac{N_n}{N_n+1}\varepsilon_{nA}. \tag{66}$$

Rearranging equation (66) and taking the logarithm,

$$\log_{10}\left|\varepsilon_n^q - \varepsilon_{ref} - \frac{N_n}{N_n+1}\varepsilon_{nA}\right| = q\log_{10}\left(\frac{1}{N_n}\right) + \log_{10}\left|\varepsilon_n^0 - \varepsilon_{ref} - \frac{N_n}{N_n+1}\varepsilon_{nA}\right|. \tag{67}$$

For $N_n \gg 1$,

$$\log_{10}\left|\varepsilon_n^q - \varepsilon_{ref} - \varepsilon_{nA}\right| = q\log_{10}\left(\frac{1}{N_n}\right) + \log_{10}\left|\varepsilon_n^0 - \varepsilon_{ref} - \varepsilon_{nA}\right|. \tag{68}$$

Equation (68) shows the error convergence relationship for the special case for which, $\lambda_{n,max} = \frac{1}{N_n}$ (thus $\lambda_{n,max} < 1$) and $C_{n,max} = \varepsilon_n^0 - \varepsilon_{ref} - \varepsilon_{nA}$. The slope $\log_{10}\left(\frac{1}{N_n}\right)$ does not depend on the initial condition $\left(p_n^0\right)$ nor the noise level on the pressure gradient. Figures 15(a-ii) and (b-ii) illustrate this behavior by means of the original omnidirectional method.

Appendix B

As indicated in figure 4, for a fixed sufficiently small distance between parallel rays, the decrease of the rotation angle increment $\Delta\alpha$ results in an improved uniform distribution of the weight function $w(l,n)$ (with $|w(l,n)| \ll 1$). As revealed by equations (14) and (15), a denser parallel ray setting means more boundary pressure point are connecting to each other. For a fixed boundary point (s_n), to ensure every boundary nodal point (s_l) has at least one chance to connect to other boundary point (s_n), simple trigonometric analyses as shown in figure 22(a) by considering the diagonal corner points A and B and the immediate neighbouring point C allow the smallest rotation angle increment $\Delta\alpha$ be estimated using the law of cosines as follows:

$$\Delta\alpha = \operatorname{acos}\left(\frac{|AB|^2 + |AC|^2 - |BC|^2}{2|AB|\cdot|AC|}\right). \tag{69}$$

For a domain with $m \times n$ nodal points and uniform grid size of Δh:

$$|AB| = \Delta h\sqrt{(m-1)^2 + (n-1)^2} \tag{70}$$

$$|AC| = \Delta h\sqrt{(m-2)^2 + (n-1)^2} \tag{71}$$

$$|BC| = \Delta h. \tag{72}$$

Plugging equations (70–72) into equation (69), we have

$$\Delta\alpha = \operatorname{acos}\left(\frac{(m-1)^2 + 2(n-1)^2 + (m-2)^2 - 1}{2\sqrt{(m-1)^2 + (n-1)^2}\cdot\sqrt{(m-2)^2 + (n-1)^2}}\right). \tag{73}$$

Thus for a domain with 254×254 nodal points, equation (62) indicates that, considering the rotational angle increment changes only, in order to ensure every boundary nodal point has at least one chance to connect to other boundary point, the minimum rotational angle increment must satisfy $\Delta\alpha \approx 0.11°$.

The optimal parallel ray line spacing Δd can be determined by considering a special case of parallel rays passing through corner neighboring points D, E and F along a 45° direction with respect to the horizontal axis of the domain, as shown in figure 22(b). In this case, in order for points D and F to be connected to each other, simple rotation of the parallel rays may not be sufficient. Rather, we need to require parallel rays adopt an optimal spacing so that the two points can be connected. Study of the geometry indicates that $\sqrt{2}/4 < \Delta d^* \equiv \Delta d/\Delta h < \sqrt{2}/2$, i.e. $0.35 < \Delta d^* < 0.71$ can ensure points D and F be connected for this case.

The above ranges for Δd^* and $\Delta\alpha$ are consistent with the parameter optimization study by Liu *et al* [15], regarding the optimum choices of line spacing Δd^* and line rotation angle increment $\Delta\alpha$. Since the above Δd^* and $\Delta\alpha$ ranges are derived separately, when combing them together, the stringent requirement may be relaxed to some extent. In this paper, we choose $\Delta d^* = 0.4$ and $\Delta\alpha = 0.2$ as a compromise between computation cost and accuracy requirement for the domain of 254×254 nodal points.

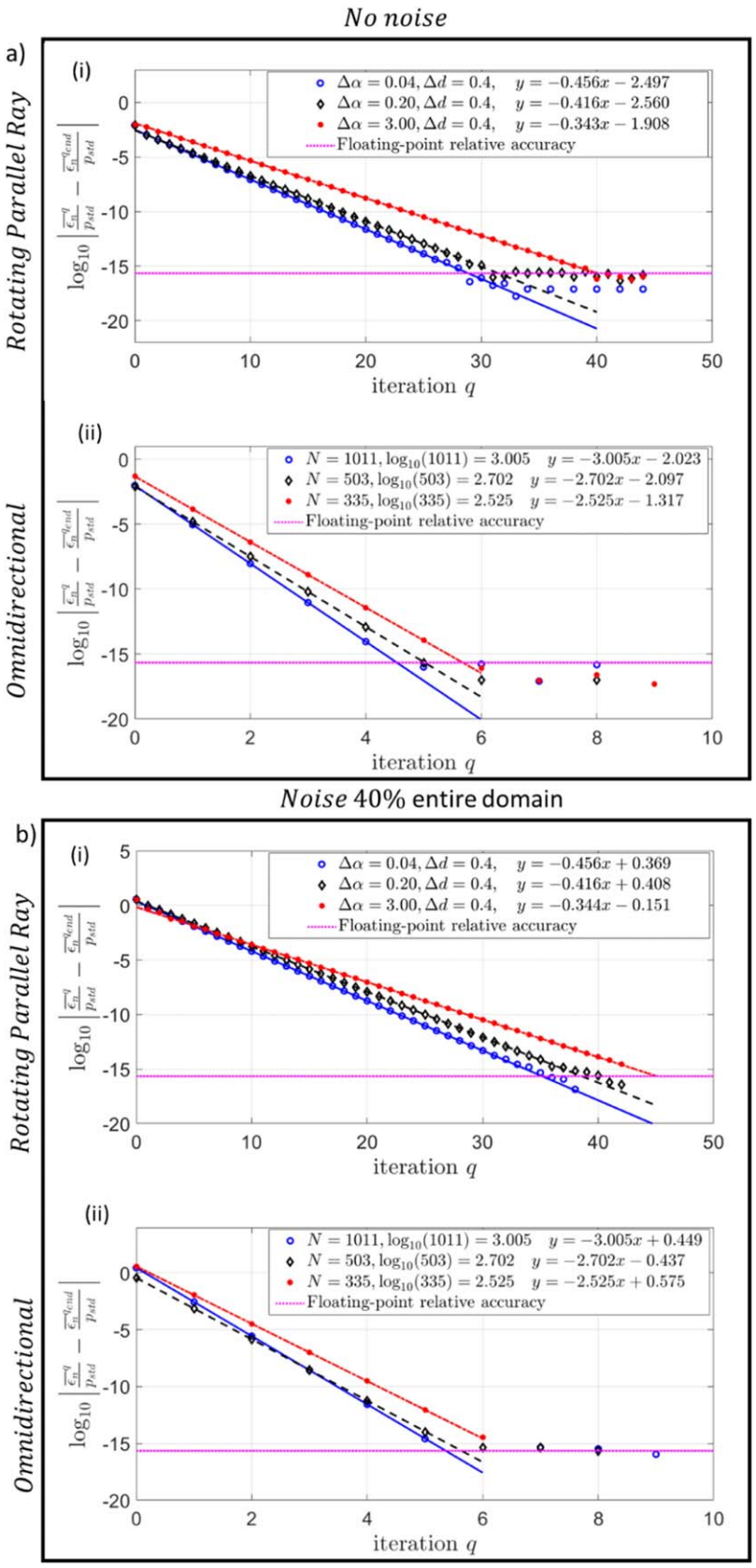

Figure 21. Boundary pressure error convergence for the pressure reconstructed from a pressure gradient field (a) without added noise and (b) with the 40% embedded noise, respectively. (a-i), and (b-i): Boundary pressure convergence using the rotating parallel ray omnidirectional integration method with three different rotational angle increments; (a-ii) and (b-ii): boundary pressure convergence using the original omnidirectional integration method [8] with three different grid size (with the same domain size but different cell size): N = 1011 corresponding to a grid of (254 × 254); N = 503 corresponding to a grid of (127 × 127), achieved by sampling every other point over the original grid; and N = 335 corresponding to (85 × 85), achieved by skipping two points for sampling.

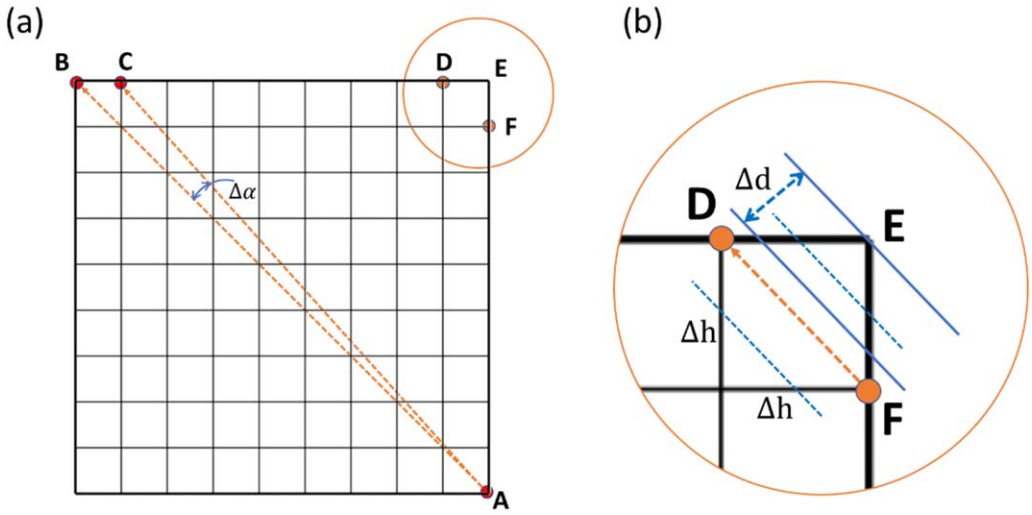

Figure 22. Schematic for optimal rotation angle increment $\Delta\alpha$ and parallel ray spacing Δd analysis.

ORCID iD

Xiaofeng Liu https://orcid.org/0000-0001-9800-6870

References

[1] Blake W K 1986 *Mechanics of Flow-induced Sound and Vibration* (New York: Academic)

[2] Girimaji S S 2000 Pressure–strain correlation modelling of complex turbulent flows *J. Fluid Mech.* **422**

[3] Liu X and Katz J 2018 Pressure–rate-of-strain, pressure diffusion, and velocity–pressure-gradient tensor measurements in a cavity flow *AIAA J.* **56** 3897–914

[4] Pope S B 2000 *Turbulent Flows* (Cambridge: Cambridge University Press)

[5] Arndt R E A 2002 Cavitation in vortical flow *Annu. Rev. Fluid Mech.* **34** 143–75

[6] Brennen C E 1995 *Cavitation and Bubble Dynamics* (New York: Oxford University Press)

[7] Liu X and Katz J 2006 Instantaneous pressure and material acceleration measurements using a four-exposure PIV system *Exp. Fluids* **41** 227–40

[8] Liu X and Katz J 2003 Measurements of pressure distribution by integrating the material acceleration *5th Int. Symp. on Cavitation* (*Osaka, Japan*)

[9] Liu X and Katz J 2007 A comparison of cavitation inception index measurements to the spatial pressure distribution within a 2D cavity shear flow *FEDSM2007-37090, 5th Joint ASME/JSME Fluids Engineering Conf.* pp 1–11

[10] Liu X and Katz J 2008 Cavitation phenomena occurring due to interaction of shear layer vortices with the trailing corner of a two-dimensional open cavity *Phys. Fluids* **20** 041702

[11] Joshi P, Liu X and Katz J 2014 Effect of mean and fluctuating pressure gradients on boundary layer turbulence *J. Fluid Mech.* **748** 36–84

[12] Liu X and Katz J 2013 Vortex-corner interactions in a cavity shear layer elucidated by time-resolved measurements of the pressure field *J. Fluid Mech.* **728** 417–57

[13] van Oudheusden B W 2008 Principles and application of velocimetry-based planar pressure imaging in compressible flows with shocks *Exp. Fluids* **45** 657–74

[14] Ragni D, Ashok A, van Oudheusden B W and Scarano F 2009 Surface pressure and aerodynamic loads determination of a transonic airfoil based on particle image velocimetry *Meas. Sci. Technol.* **20** 074005

[15] Liu X, Moreto J R and Siddle-Mitchell S 2016 Instantaneous pressure reconstruction from measured pressure gradient using rotating parallel ray method *54th AIAA Aerospace Sciences Meeting* (Reston, VA: American Institute of Aeronautics and Astronautics)

[16] Zhang C, Wang J, Blake W and Katz J 2017 Deformation of a compliant wall in a turbulent channel flow *J. Fluid Mech.* **823** 345–90

[17] Dabiri J O, Bose S, Gemmell B J, Colin S P and Costello J H 2014 An algorithm to estimate unsteady and quasi-steady pressure fields from velocity field measurements *J. Exp. Biol.* **217** 331–6

[18] Wang Z, Gao Q, Wang C, Wei R and Wang J 2016 An irrotation correction on pressure gradient and orthogonal-path integration for PIV-based pressure reconstruction *Exp. Fluids* **57** 104

[19] de Kat R and van Oudheusden B W 2012 Instantaneous planar pressure determination from PIV in turbulent flow *Exp. Fluids* **52** 1089–106

[20] de Kat R and Van Oudheusden B W 2010 Instantaneous planar pressure from PIV: analytic and experimental test-cases *15th Int. Symp. on Applications of Laser Techniques to Fluid Mechanics*

[21] Violato D, Moore P and Scarano F 2011 Lagrangian and Eulerian pressure field evaluation of rod-airfoil flow from time-resolved tomographic PIV *Exp. Fluids* **50** 1057–70

[22] van Oudheusden B W 2013 PIV-based pressure measurement *Meas. Sci. Technol.* **24** 032001

[23] Auteri F, Carini M, Zagaglia D, Montagnani D, Gibertini G, Merz C B and Zanotti A 2015 A novel approach for reconstructing pressure from PIV velocity measurements *Exp. Fluids* **56** 45

[24] Haigermoser C 2009 Application of an acoustic analogy to PIV data from rectangular cavity flows *Exp. Fluids* **47** 145–57

[25] Koschatzky V, Westerweel J and Boersma B J 2011 A study on the application of two different acoustic analogies to experimental PIV data *Phys. Fluids* **23** 065112

[26] Liu X and Katz J 2011 Time resolved measurements of the pressure field generated by vortex-corner interactions in a cavity shear layer *Proc. ASME-JSME-KSME Joint Fluids Engineering Conf. (Hamamatsu, Shizuoka, Japan, 24–29 July)*

[27] Moore P, Lorenzoni V and Scarano F 2011 Two techniques for PIV-based aeroacoustic prediction and their application to a rod-airfoil experiment *Exp. Fluids* **50** 877–85
[28] Jeon Y J, Chatellier L, Beaudoin A and David L 2015 Least – square reconstruction of instantaneous pressure field around a body based on a directly acquired material acceleration in time – resolved PIV *11th Int. Symp. Part. Image Velocim.*
[29] Wang C Y, Gao Q, Wei R J, Li T and Wang J J 2017a Spectral decomposition-based fast pressure integration algorithm *Exp. Fluids* **58** 84
[30] Tronchin T, David L and Farcy A 2015 Loads and pressure evaluation of the flow around a flapping wing from instantaneous 3D velocity measurements *Exp. Fluids* **56** 7
[31] Neeteson N J and Rival D E 2015 Pressure-field extraction on unstructured flow data using a Voronoi tessellation-based networking algorithm: a proof-of-principle study *Exp. Fluids* **56** 44
[32] Schanz D, Gesemann S and Schröder A 2016 Shake-The-Box: lagrangian particle tracking at high particle image densities *Exp. Fluids* **57** 70
[33] Huhn F, Schanz D, Gesemann S and Schröder A 2016 FFT integration of instantaneous 3D pressure gradient fields measured by Lagrangian particle tracking in turbulent flows *Exp. Fluids* **57**
[34] Charonko J J, King C V, Smith B L and Vlachos P P 2010 Assessment of pressure field calculations from particle image velocimetry measurements *Meas. Sci. Technol.* **21** 105401
[35] van Gent P L *et al* 2017 Comparative assessment of pressure field reconstructions from particle image velocimetry measurements and Lagrangian particle tracking *Exp. Fluids* **58** 33
[36] de Kat R and Ganapathisubramani B 2013 Pressure from particle image velocimetry for convective flows: a Taylor's hypothesis approach *Meas. Sci. Technol.* **24** 024002
[37] McClure J and Yarusevych S 2017b Optimization of planar PIV-based pressure estimates in laminar and turbulent wakes *Exp. Fluids* **58** 62
[38] Lynch K P and Scarano F 2014 Material acceleration estimation by four-pulse tomo-PIV *Meas. Sci. Technol.* **25** 084005
[39] Wieneke B 2015 PIV uncertainty quantification from correlation statistics *Meas. Sci. Technol.* **26** 074002
[40] Sciacchitano A and Wieneke B 2016 PIV uncertainty propagation *Meas. Sci. Technol.* **27** 084006
[41] Wang Z, Gao Q, Wei R and Wang J 2017b Error propagation in the procedure of pressure reconstruction based on PIV data *J. Phys. Conf. Ser.* **822** 012055
[42] Gomit G, Acher G, Chatellier L and David L 2018 Uncertainty analysis of an optical method for pressure estimation in fluid flows *Meas. Sci. Technol.* **29** 024004
[43] van Gent P L, Schrijer F F J and van Oudheusden B W 2018a Assessment of the pseudo-tracking approach for the calculation of material acceleration and pressure fields from time-resolved PIV: part I. Error propagation *Meas. Sci. Technol.* **29** 045204
[44] van Gent P L, Schrijer F F J and van Oudheusden B W 2018b Assessment of the pseudo-tracking approach for the calculation of material acceleration and pressure fields from time-resolved PIV: part II. Spatio-temporal filtering *Meas. Sci. Technol.* **29** 045206
[45] Pan Z, Whitehead J, Thomson S and Truscott T 2016 Error propagation dynamics of PIV-based pressure field calculations: how well does the pressure Poisson solver perform inherently? *Meas. Sci. Technol.* **27** 084012
[46] Liu X and Moreto J R 2019 Error propagation from the PIV-based pressure gradient to the integrated pressure by the omni-directional integration method *(ISPIV, Munich, Germany, 22–24 July 2019)* https://athene-forschung.unibw.de/doc/129117/129117.pdf
[47] Gurka R, Liberzon A, Hefetz D, Rubinstein D and Shavit U 1999 Computation of pressure distribution using PIV velocity data *Workshop on Particle Image Velocimetry* vol 2, pp 1–6
[48] Jensen A, Pedersen G K and Wood D J 2003 An experimental study of wave run-up at a steep beach *J. Fluid Mech.* **486** 161–88
[49] Jensen A and Pedersen G K 2004 Optimization of acceleration measurements using PIV *Meas. Sci. Technol.* **15** 2275–83
[50] Baur T and Kongeter J 1999 PIV with high temporal resolution for the determination of local pressure reductions from turbulent phenomena *11th Int. Symp. on Particle Image Velocimetry (Santa Barbara, CA, USA, 14–16 September 2015)*
[51] Wang J, Zhang C and Katz J 2019 GPU-based, parallel-line, omnidirectional integration of measured pressure gradient field to obtain the 3D pressure distribution *Exp. Fluids* **60** 58
[52] Huang H, Dabiri D and Gharib M 1997 On errors of digital particle image velocimetry *Meas. Sci. Technol.* **8** 1427
[53] Roth G I and Katz J 2001 Five techniques for increasing the speed and accuracy of PIV interrogation *Meas. Sci. Technol.* **12** 238
[54] Perlman E, Burns R, Li Y and Meneveau C 2007 Data exploration of turbulence simulations using a database cluster *Proc. 2007 ACM/IEEE Conf. on Supercomputing—SC '07* (New York, USA: ACM Press)
[55] Li Y, Perlman E, Wan M, Yang Y, Meneveau C, Burns R, Chen S, Szalay A and Eyink G 2008 A public turbulence database cluster and applications to study Lagrangian evolution of velocity increments in turbulence *J. Turbul.* **9**
[56] Graham J, Lee M, Malaya N, Moser R D, Eyink G, Meneveau C, Kanov K, Burns R, Szalay A and Idies 2013 *Turbulent Channel Flow Data Set*
[57] Gerald C F and Wheatley P O 2004 *Applied Numerical Analysis* 7th edn (New York: Pearson Education)
[58] Ghaemi S, Ragni D and Scarano F 2012 PIV-based pressure fluctuations in the turbulent boundary layer *Exp. Fluids* **53** 1823–40
[59] Ghaemi S and Scarano F 2013 Turbulent structure of high-amplitude pressure peaks within the turbulent boundary layer *J. Fluid Mech.* **735** 381–426
[60] Villegas A and Diez F J 2014 Evaluation of unsteady pressure fields and forces in rotating airfoils from time-resolved PIV *Exp. Fluids* **55** 1–17
[61] Neeteson N J, Bhattacharya S, Rival D E, Michaelis D, Schanz D and Schröder A 2015 Pressure-field extraction from Lagrangian flow measurements *11th Int. Symp. on Particle Image Velocimetry (Santa Barbara, CA, USA, 14–16 September 2015)*
[62] Löhrer B, Valiorgue P, Ben Hadid H, Fröhlich J and Doppler D 2015 Pressure measurements using particle image velocimetry in the vicinity of a flexible moving structure *11th Int. Symp. on Particle Image Velocimetry (Santa Barbara, CA, USA, 14–16 September 2015)*
[63] Mariconda C and Tonolo A 2016 *Discrete Calculus* vol 103 (Cham: Springer International Publishing)